Potential quantum advantage for simulation of fluid dynamics

Xiangyu Li,[1, *] Xiaolong Yin,[2] Nathan Wiebe,[3, 1, 4] Jaehun Chun,[1, 5] Gregory
K. Schenter,[1] Margaret S. Cheung,[1, 6] and Johannes Mülmenstädt[1, †]

[1]*Pacific Northwest National Laboratory, Richland, WA, USA*
[2]*Petroleum Engineering, Colorado School of Mines, Golden, CO, USA*
[3]*Department of Computer Science, University of Toronto, Toronto, ON, Canada*
[4]*Canadian Institute for Advanced Research, Toronto, ON, Canada*
[5]*Levich Institute and Department of Chemical Engineering,*
CUNY City College of New York, New York, NY, USA
[6]*Department of Physics, University of Washington, Seattle, WA, USA*

Numerical simulation of turbulent fluid dynamics needs to either parameterize turbulence—which introduces large uncertainties—or explicitly resolve the smallest scales—which is prohibitively expensive. Here we provide evidence through analytic bounds and numerical studies that a potential quantum exponential speedup can be achieved to simulate the Navier–Stokes equations governing turbulence using quantum computing. Specifically, we provide a formulation of the lattice Boltzmann equation for which we give evidence that low-order Carleman linearization is much more accurate than previously believed for these systems and that for computationally interesting examples. This is achieved via a combination of reformulating the nonlinearity and accurately linearizing the dynamical equations, effectively trading nonlinearity for additional degrees of freedom that add negligible expense in the quantum solver. Based on this we apply a quantum algorithm for simulating the Carleman-linerized lattice Boltzmann equation and provide evidence that its cost scales logarithmically with system size, compared to polynomial scaling in the best known classical algorithms. This work suggests that an exponential quantum advantage may exist for simulating fluid dynamics, paving the way for simulating nonlinear multiscale transport phenomena in a wide range of disciplines using quantum computing.

INTRODUCTION

Complex systems exhibiting multiscale dynamics are ubiquitous in nature. Developing the ability to understand, predict, or modify these systems ranks among the "grand challenges" of science and engineering [1–3]. Areas of application for this knowledge include the Earth's ocean and atmosphere [4–8], biological systems [9], and synthesis of advanced materials [10–14]. The dynamics of these systems admits no analytic solution, but numerical simulation needs to either parameterize the small-scale processes—which introduces large uncertainties—or explicitly resolve the smallest scales—which is prohibitively expensive.

Turbulent fluid dynamics embodies a defining feature of complex systems: the lack of scale separation [15, 16]. As all scales interact with each other, they cannot be investigated individually. Turbulence contributes to the multiscale behavior of many of the complex systems mentioned above, including geophysical [17–19], astrophysical, and many engineering fluid dynamics applications. Because the length and time scales of the constituent processes can be a minute fraction of the integral scale of the system (e.g., the turbulent length scale range is $\sim 10^7$ for atmospheric flows), outright scale range-resolving simulations are simply not feasible on classical computers [20, 21].

Attempts to understand turbulence have centered on the Navier–Stokes equations (NSE). These equations describe the macroscopic momentum and density evolution of fluids; multiscale interactions arise from the nonlinear advection term $\mathbf{u} \cdot \nabla \mathbf{u}$ for the fluid velocity field $\mathbf{u}(\mathbf{x}, \mathbf{t})$ in space $\mathbf{x}$ and time t (see Methods). Approaches to solving the NSE numerically include using "reduced" models that are based on a proper orthogonal decomposition with key representative modes to mimic the dynamics of the full spectrum [22, 23] and averaging over those scales not explicitly resolved (e.g., with Reynolds averaging) and using a constitutive relation (e.g., eddy viscosity) to close the Reynolds-averaged NSE [24, 25]. Such approaches parameterize the small-scale behavior based on the resolved-scale state of the model, which produces tractable simulations at the expense of an artificial scale separation. This unavoidable model defect results in persistent uncertainty in projections of complex systems' emergent behaviors [4, 26, 27], e.g., the sensitivity of the climate to anthropogenic perturbations [28–34].

A structurally different formulation of fluid dynamics exists in the form of the Boltzmann equation. This formulation describes the evolution of particle distribution functions $f(\mathbf{x}, \mathbf{v}, t)$ in space and particle velocity $\mathbf{v}$ (see Eq. (7) and

* xiangyu.li@pnnl.gov
† johannes.muelmenstaedt@pnnl.gov

Eq. (17) in Methods). These distribution functions are mesoscopic objects that comprise sufficiently large numbers of molecules for a statistical-mechanics treatment but that are smaller than the macroscopic fluid elements. The Boltzmann equation is still nonlinear (see below), but in an important difference from the NSE, its nonlinearity does not reside in the advection term [35]. In classical time-marching spectral or spatial discretization algorithms, the Boltzmann equation is even more prohibitively expensive than the NSE [36]; in quantum computing algorithms, as we will show, the trade-off goes the other way, largely due to the linear Boltzmann advection term.

Requirements for Quantum Algorithm

Whether the NSE or Boltzmann equation is chosen, explicit simulation of turbulence requires large numbers of degrees of freedom N. In both spatial and spectral discretization, N reflects the ratio between the largest and smallest scales, i.e., the integral system scale and the Kolmogorov scale. As quantum computers inherently grant the ability to manipulate vectors in exponentially large vector spaces in polynomial time, one may ask whether such methods could be used to solve the turbulence problem.

Harrow, Hassidim, and Lloyd [37] answer this question in the affirmative for generic linear systems. This vector manipulation approach naturally leads to a strategy for achieving a potential exponential speedup when solving systems of coupled ordinary differential equations [38, 39] . Specifically, these quantum linear system algorithms can yield a state $|x\rangle$ for any $|b\rangle$ solved for a sparse Hermitian matrix A such that the equation

$$A|x\rangle = |b\rangle \tag{1}$$

is satisfied up to a constant of proportionality. The method works by constructing a unitary matrix that encodes A within a block of the original matrix, specifically, $(\langle 0| \otimes I)U_{A^{-1}}(|0\rangle \otimes I)|0\rangle|b\rangle \propto A^{-1}|b\rangle$, with I being the identity matrix. Such a representation is known as a block encoding. The performance cost scales as $O(d\kappa \log(1/\epsilon))$ accesses to the matrix elements of the d-sparse matrix A, which we further assume is invertible and has condition number κ and desired solution error ϵ [40].

The simplest strategy that can be employed for solving systems of differential equations involves using a forward-Euler approach to discretize a differential equation of the form $\partial_t x(t) = Ax(t) + b(t)$ and then solve the resulting equation using the quantum linear systems algorithm. The resulting difference equation takes the form $x(t_{i+1}) = x(t_i) + hAx(t_i) + hb(t)$ for stepsize h. The central idea behind this approach is to construct a quantum state over both the solution space and the time that the system is evaluated at. Specifically, if we let our solution be $x(t)$, then we encode our solution as $\sum_i c_i|t_i\rangle|\psi_i\rangle$, where $|\psi_i\rangle$ is the solution at time t_i, and c_i is arbitrary constants. Given a state of this form, we can find the solution state by measuring the t_i register (or using amplitude amplification) to achieve a value that is t_f, which is the final time desired for the algorithm. In practice, the probability of measuring this result is low, so the standard approach to this problem is to extend (typically double) the simulation time but turn off the differential equation to ensure that the solutions are merely copied on all subsequent times. Since the solution is the same at all such times, this serves to raise the probability of success to a constant without requiring substantial computational overhead. Specifically, the solution for a two-time-step result with two further time steps used for padding then reads [38]

$$\begin{bmatrix} I & 0 & 0 & 0 & 0 \\ -(I+hA) & I & 0 & 0 & 0 \\ 0 & -(I+hA) & I & 0 & 0 \\ 0 & 0 & -I & I & 0 \\ 0 & 0 & 0 & -I & I \end{bmatrix} \begin{bmatrix} x(0) \\ x(h) \\ x(2h) \\ x(3h) \\ x(4h) \end{bmatrix} = \begin{bmatrix} x_{\text{init}} \\ bh \\ bh \\ 0 \\ 0 \end{bmatrix} \tag{2}$$

In this form, the solution vector over all times can be found by inverting the above matrix. In practice, this approach is not favorable in classical computing, as it requires a substantial overhead due to the dimension of the space. But, as the cost of the quantum linear systems algorithms does not directly depend on the dimension, this approach can be surprisingly effective in quantum settings.

Taking the algorithm of Berry *et al.* [39] as an example, the overall algorithm complexity, as measured by the number of two-qubit quantum gates and oracle queries, depends on $\log N$, but also on numerous other properties of the system of equations being solved (expressed through the $N \times N$ coefficient matrix $\mathcal{C}$):

$$\text{gate complexity} = O(\|\mathcal{C}\|\kappa_J gTs \cdot \text{poly}(\log(\kappa_J sg\beta T\|\mathcal{C}\|N/\epsilon))). \tag{3}$$

These properties include the spectral norm of the coefficient matrix $\|\mathcal{C}\|$, the condition number κ_J of the eigenvectors

Navier–Stokes

(a)

$$\frac{\partial \mathbf{u}}{\partial t} + \mathbf{u} \cdot (\nabla \mathbf{u}) = -\frac{\nabla p}{\rho} + \nu \nabla^2 \mathbf{u} + \mathbf{F}$$

$$\mathbf{u} \cdot (\nabla \mathbf{u})/(\nu \nabla^2 \mathbf{u}) \sim \mathrm{Re} \gg 1$$

$$N = O(n)$$

**Reynolds-determined
strong nonlinearity**

(b)

*Weakening
Nonlinearity*

Fails for Re > O(1) . . .

Lattice Boltzmann

$$\frac{\partial f}{\partial t} + \mathbf{e} \cdot \frac{\partial}{\partial \mathbf{x}} f = \Omega(f)$$

$$|\langle \mathbf{e}f \rangle/\langle f \rangle| \sim O(\mathrm{Ma}) \ll 1$$

$$N = O(nQ)$$

**Mach-determined
weak nonlinearity**

Linearizing

(c)

Carleman Linearized LBE

$$\frac{\partial V^{(k)}(\mathbf{x})}{\partial t} = \left[\begin{pmatrix} A_1^1(\mathbf{x}) & A_2^1(\mathbf{x}) & A_3^1(\mathbf{x}) & 0 & 0 & \dots & 0 & 0 & 0 & 0 \\ 0 & A_2^2(\mathbf{x}) & A_3^2(\mathbf{x}) & A_4^2(\mathbf{x}) & 0 & \dots & 0 & 0 & 0 & 0 \\ \vdots & \vdots & \vdots & \vdots & \vdots & \ddots & \vdots & \vdots & \vdots & \vdots \\ 0 & 0 & 0 & 0 & 0 & \dots & 0 & A_{k-2}^{k-2}(\mathbf{x}) & A_{k-1}^{k-2}(\mathbf{x}) & A_k^{k-2}(\mathbf{x}) \\ 0 & 0 & 0 & 0 & 0 & \dots & 0 & 0 & A_{k-1}^{k-1}(\mathbf{x}) & A_k^{k-1}(\mathbf{x}) \\ 0 & 0 & 0 & 0 & 0 & \dots & 0 & 0 & 0 & A_k^k(\mathbf{x}) \end{pmatrix} \right.$$

$$\left. - \begin{pmatrix} B_1^1 & 0 & 0 & 0 & 0 & \dots & 0 & 0 & 0 & 0 \\ 0 & B_2^2 & 0 & 0 & 0 & \dots & 0 & 0 & 0 & 0 \\ \vdots & \vdots & \vdots & \vdots & \vdots & \ddots & \vdots & \vdots & \vdots & \vdots \\ 0 & 0 & 0 & 0 & 0 & \dots & 0 & B_{k-2}^{k-2} & 0 & 0 \\ 0 & 0 & 0 & 0 & 0 & \dots & 0 & 0 & B_{k-1}^{k-1} & 0 \\ 0 & 0 & 0 & 0 & 0 & \dots & 0 & 0 & 0 & B_k^k \end{pmatrix} \right] V^{(k)}(\mathbf{x})$$

$$N = O(n^3 Q^3)$$

**no efficient
quantum
algorithms . . .**

(d)

**Linearized system
with many degrees
of freedom suitable
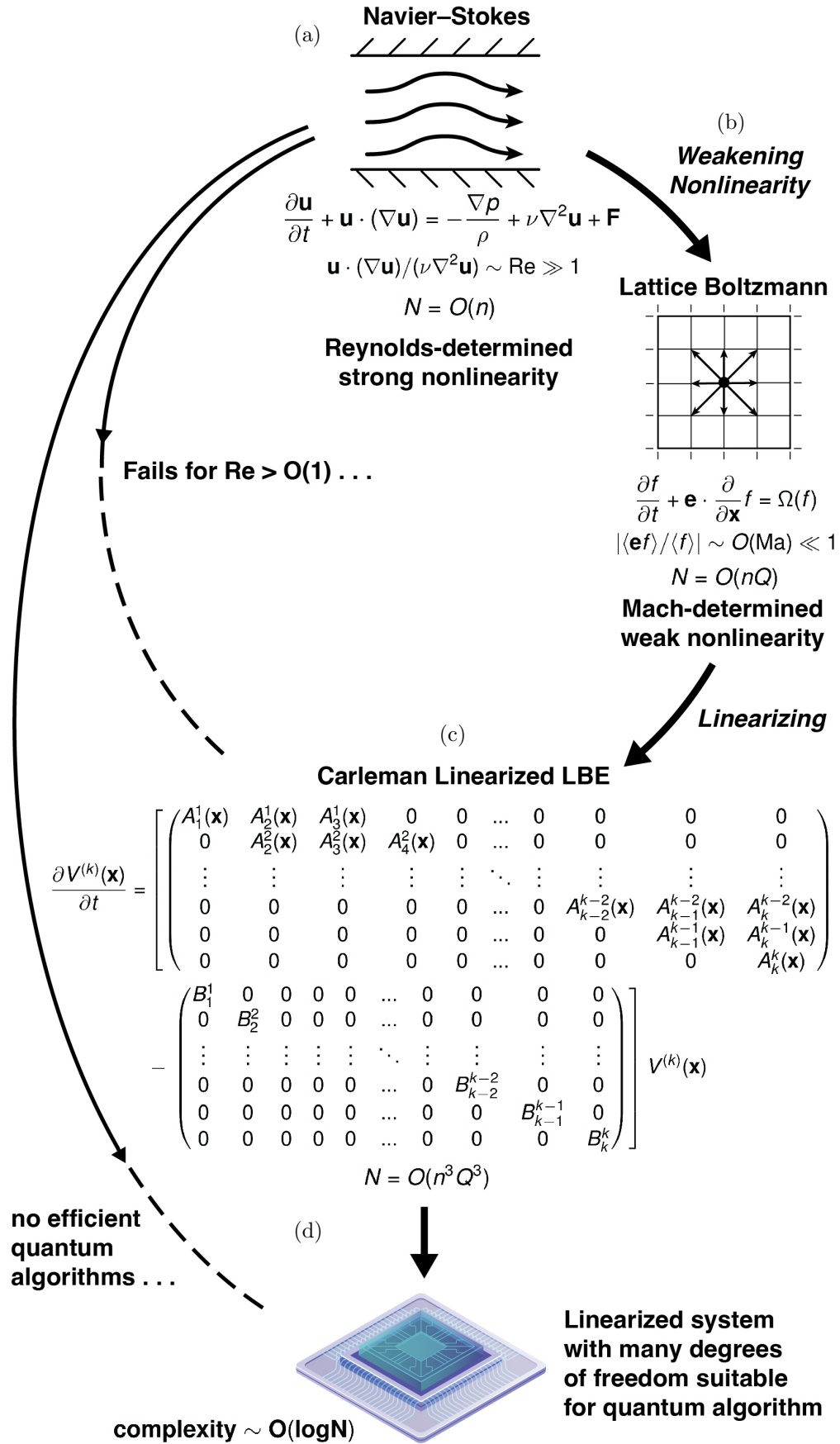for quantum algorithm**

complexity $\sim O(\log N)$

FIG. 1. Illustration of the complexity of solving Navier–Stokes equations using quantum algorithms: (a) Reynolds number-determined strongly nonlinear Navier–Stokes equations; (b) Mach number-determined weak nonlinear lattice Boltzmann form of Navier–Stokes equations; (c) Carleman-linearized lattice Boltzmann equation; (d) exponential quantum advantage in solving the Carleman-linearized lattice Boltzmann equation.

of $\mathcal{C}$, the dissipation parameter g, the evolution time T, the sparsity s, the norm of the initial state β, and the desired solution error ϵ. If any of $\|\mathcal{C}\|$, κ_J, g, T, or s has implicit polynomial (or worse) dependence on N, or if β or ϵ has exponential (or worse) dependence on N, the headline exponential advantage is negated.

When the underlying system of equations is nonlinear, the requirements for efficient solution become more stringent still. There is no known quantum algorithm that is directly applicable to nonlinear differential equations; instead, the nonlinear system first needs to be approximated by a (larger) system of linear equations [41, 42]. Whether the quantum algorithm is still efficient after this approximation depends on the degree of nonlinearity [42]. The nonlinearity of NSE is characterized by the Reynolds number (see Methods). Quantum algorithms are unable to simulate NSE [42] with $\mathrm{Re} \geq \sqrt{2}$, which is far from the values in relevant cases (e.g., atmospheric turbulence [43, 44] with $\mathrm{Re} \approx 10^7$).

We will now analyze whether the Boltzmann form of fluid dynamics, after linearization, can take advantage of quantum algorithms' efficient handling of large N without violating these algorithms' strict requirements. Our aim in this manuscript is not quantum algorithm development but, rather, showing that turbulent fluid dynamics is tractable with existing quantum algorithms, provided the Boltzmann formulation, rather than the NSE formulation, is used.

METHODS

Navier–Stokes equations and their lattice Boltzmann form

The Navier–Stokes equations (NSE) governing fluid dynamics read

$$\frac{\partial \mathbf{u}}{\partial t} + \mathbf{u} \cdot (\nabla \mathbf{u}) = -\frac{\nabla p}{\rho} + \nu \nabla^2 \mathbf{u} + \mathbf{F}, \tag{4}$$

$$\frac{\partial \rho}{\partial t} + \nabla \cdot (\rho \mathbf{u}) = 0, \tag{5}$$

where $\mathbf{u}$ is the flow velocity, p is the pressure, ρ is the fluid density, ν is the kinematic viscosity, and $\mathbf{F}$ is the forcing term. The nonlinearity of Eq. (4) is exhibited in $\mathbf{u} \cdot (\nabla \mathbf{u})$. This term and the viscosity term $\nu \nabla^2 \mathbf{u}$ together determine the multiscale property of a turbulent flow characterized by the Reynolds number $\mathrm{Re} = \mathbf{u} \cdot (\nabla \mathbf{u})/(\nu \nabla^2 \mathbf{u})$. Flow systems in nature are often characterized by high Re (e.g., $\mathrm{Re} \approx 10^7$ for atmospheric flows and $\mathrm{Re} \approx 10^{21}$ for astrophysical flows), which are intractable to simulate using classical computers, as the best-case computational cost scales as Re^3 according to the Kolmogorov theory[15]. The compressibility of the flow is characterized by the Mach number $\mathrm{Ma} = |\mathbf{u}|/c_s$ with c_s being the speed of sound.

We solve the lattice Boltzmann form of the NSE to reduce the nonlinearity from Re-determined $\mathbf{u} \cdot (\nabla \mathbf{u})$ to Ma-determined $u^2 = \mathbf{u} \cdot \mathbf{u}$. The discrete-velocity Boltzmann form of Eq. (4) with Bhatnagar–Gross–Krook (BGK) collision [45] leads to:

$$\frac{\partial \tilde{f}_m}{\partial \tilde{t}} + \tilde{\mathbf{e}}_m \cdot \tilde{\nabla} \tilde{f}_m = -\frac{1}{\tilde{\tau}} \left(\tilde{f}_m - \tilde{f}_m^{\mathrm{eq}} \right), \quad m \in 1, \ldots, Q, \tag{6}$$

where $\tilde{f}_m(\tilde{\mathbf{x}}, \tilde{t})$ is the particle velocity distribution function describing the probability density of finding a particle around position $\tilde{\mathbf{x}}$ at time $\tilde{t}$ with unit discrete velocity $\tilde{\mathbf{e}}_m$, and Q is the number of discrete velocities [35]. If a spatial discretization uses n grid points, the dimensionality of f is $n \times Q$; as we will discuss below, Q is a fixed, small number ($Q \leq 27$ in widespread practice), whereas simulations with large domains or fine resolutions are often desirable, resulting in $n \gg 1$. In our complexity analysis, we therefore treat Q as a constant and n as a parameter of the problem whose effects in the large-n limit are of particular practical interest. In one, two, and three dimensions, the square or cubic lattices D1Q3, D2Q9, and D3Q27 are in widespread use [35]. $\tilde{f}_m^{\mathrm{eq}}$ is the local Maxwell equilibrium that $\tilde{f}_m(\mathbf{x}, t)$ relaxes to at a relaxation time of $\tilde{\tau}$. $\tilde{\nabla}$ represents the spatial gradient in the $\tilde{x}$, $\tilde{y}$, and $\tilde{z}$ directions. By using a reference density ρ_r and speed e_r, characteristic macroscopic length scale L, and particle collision t_c, one obtains the nondimensional form of Eq. (6), termed the lattice Boltzmann equation (LBE):

$$\partial_t f_m + \mathbf{e}_m \cdot \nabla f_m = -\frac{1}{\tau \, \mathrm{Kn}} (f_m - f_m^{\mathrm{eq}}), \quad m = 1, \ldots, Q, \tag{7}$$

where

$$f_m = \tilde{f}_m/\rho_r, \tag{8}$$

$$f_m^{\text{eq}} = \tilde{f}_m^{\text{eq}}/\rho_r, \tag{9}$$

$$t = \tilde{t}/(L/e_r), \tag{10}$$

$$\mathbf{e} = \tilde{\mathbf{e}}/e_r, \tag{11}$$

$$\nabla = L\tilde{\nabla}, \text{ and} \tag{12}$$

$$\tau = \tilde{\tau}/t_c. \tag{13}$$

(To minimize clutter in the following, variables without tilde are nondimensional, and variables with tilde are their dimensional physical counterparts.) The Knudsen number describing the ratio of collision time to flow time is defined as

$$\text{Kn} = e_r \frac{t_c}{L} \tag{14}$$

and forms the basis for the Chapman–Enskog expansion [35] of the LBE, which recovers the NSE in the limit $\text{Kn} \ll 1$. The macroscopic fluid density $\rho(\mathbf{x}, t)$ is retrieved as

$$\rho(\mathbf{x}, t) = \sum_m f_m(\mathbf{x}, t) \tag{15}$$

and the macroscopic fluid velocity as

$$\mathbf{u}(\mathbf{x}, t) = \frac{1}{\rho} \sum_m f_m(\mathbf{x}, t)\mathbf{e}_m. \tag{16}$$

To recover the NSE from Eq. (7), the equilibrium distribution function $f_m(\mathbf{x}, t)$ is chosen as the Taylor expansion of the Maxwell distribution function:

$$f_m^{\text{eq}} = \rho w_m[a + b\mathbf{e}_m \cdot \mathbf{u} + c(\mathbf{e}_m \cdot \mathbf{u})^2 + d|\mathbf{u}|^2]; \tag{17}$$

quadratic degree enables the LBE to reproduce the quadratic NSE to $O(\text{Ma}^2)$, and the constants $a = 1$, $b = 3$, $c = 9/2$, and $d = -3/2$ are the Taylor coefficients [35].

Constants a through d are all $O(1)$ quantities as, in the lattice Boltzmann method (LBM), they are proportional to the powers of the speed of sound, which is $O(1)$ due to the velocity rescaling. The lattice constants $w_1, \ldots, w_Q$ provide the Maxwell weighting of the different discrete velocities $\mathbf{e}_1, \ldots, \mathbf{e}_Q$ (which are not necessarily unit vectors) and satisfy

$$\sum_m w_m = 1. \tag{18}$$

The lattice constants depend on the dimension $D \in \{1, 2, 3\}$ of the simulation and the number Q of discrete velocities used. As the speed of sound is $O(1)$, the macroscopic velocity $|\mathbf{u}| = O(\text{Ma})$, i.e., $|\mathbf{u}| \ll 1$ in weakly compressible applications. We remark that the LBM is suitable for high Reynolds number flow since the condition of $\text{Kn} = O(\text{Ma/Re})$ can be well met [46] with $\text{Re} \gg 1$. This feature of LBM is crucial for the complexity analysis discussed below.

Carleman linearization of the lattice Boltzmann equation

The LBE (Eq. (7)) contains terms that are nonlinear in f due to the presence of the ρu^2 terms in f_m^{eq} (i.e., Eq. (17)). These nonlinear terms involve the ratio of quadratic combinations of f_m in the numerator and linear combinations of f_m in the denominator. Because the deviation of the denominator (macroscopic density ρ) from 1 is small ($\rho \approx 1$) in weakly compressible flow, we can approximate $1/\rho$ to first-order Taylor expansion as

$$\frac{1}{\rho} \approx 2 - \rho, \quad |1 - \rho| \ll 1 \tag{19}$$

with $O(\text{Ma}^4)$ error; this is acceptable, since the LBE recovers NSE to $O(\text{Ma}^2)$. Substituting the expansion of $1/\rho$ yields polynomial combinations of f_m up to cubic degree in f_m^{eq}. Cubic degree is therefore the minimum usable Carleman degree that can recover NSE when $\text{Ma} \ll 1$.

We collect the terms of different polynomial degree in Eq. (7) after the expansion of Eq. (17), with linear terms on the first, quadratic on the second, and cubic terms on the third lines:

$$
\begin{aligned}
\frac{\partial f_m}{\partial t} = & - \mathbf{e}_m \cdot \nabla f_m - \frac{1}{\text{Kn}\tau} f_m + \frac{1}{\text{Kn}\tau} w_m \left[a \sum_{n=1}^{Q} f_n + b\mathbf{e}_m \cdot \sum_{n=1}^{Q} \mathbf{e}_n f_n \right] \\
& + \frac{2}{\text{Kn}\tau} w_m \left[c \left(\mathbf{e}_m \cdot \sum_{n=1}^{Q} \mathbf{e}_n f_n \right)^2 + d \left(\sum_{n=1}^{Q} \mathbf{e}_n f_n \right)^2 \right] \\
& - \frac{1}{\text{Kn}\tau} w_m \left[\sum_{n=1}^{Q} f_n \right] \left[c \left(\mathbf{e}_m \cdot \sum_{n=1}^{Q} \mathbf{e}_n f_n \right)^2 + d \left(\sum_{n=1}^{Q} \mathbf{e}_n f_n \right)^2 \right]
\end{aligned}
\tag{20}
$$

In the following, we adopt the Forets and Pouly [47] notation and separate the linear, quadratic, and cubic terms into products of constant coefficient matrices F_1, F_2, and F_3 and 1-, 2-, and 3-forms. Note that we will treat the streaming operator

$$
Sf = \mathbf{e}_m \cdot \nabla f_m
\tag{21}
$$

separately for reasons that will become apparent in the discussion of n-point grids. We write Eq. (20) as

$$
\frac{\partial f}{\partial t} = -Sf + F^{(1)}f + F^{(2)}f^{[2]} + F^{(3)}f^{[3]},
\tag{22}
$$

where

$$
f = (f_1, \ldots, f_Q)^{\text{T}};
\tag{23}
$$

the superscript $^{[k]}$ denotes Kronecker exponentiation:

$$
f^{[k]} = \underbrace{f \otimes \cdots \otimes f}_{k \text{ times}}
\tag{24}
$$

$f^{[k]}$ is the Q^k-length vector of polynomial permutations of f_m of degree k, including terms that are degenerate because of commutativity under multiplication. The Kronecker product operator $\otimes$ acts on vectors

$$
x \otimes y = (x_1 y_1, x_1 y_2, \ldots, x_1 y_m, x_2 y_1, \ldots, x_2 y_m, \ldots, x_n y_1, \ldots, x_n y_m)^{\text{T}}
\tag{25}
$$

and matrices

$$
A \otimes B = \begin{pmatrix} a_{11}B & \ldots & a_{1n}B \\ \vdots & & \vdots \\ a_{m1}B & \ldots & a_{mn}B \end{pmatrix}
\tag{26}
$$

by forming all product permutations of their elements. $F^{(k)}$ is a $Q \times Q^k$ matrix of constant coefficients of the polynomial combinations of f_m. The procedure of Carleman linearization [48] recasts this system of Q polynomial differential equations as an infinite system of coupled linear differential equations by treating $f^{[k]}$ as new degrees of freedom whose time derivatives are determined from Eq. (22) by the Leibniz product rule. Denoting

$$
V^{(k)} = (f, f^{[2]}, \ldots, f^{[k]})^{\text{T}},
\tag{27}
$$

the infinite-dimensional Carleman form of Eq. (22) reads

$$
\frac{\partial V^{(\infty)}}{\partial t} = C^{(\infty)} V^{(\infty)},
\tag{28}
$$

with

$$
C^{(\infty)} = \begin{pmatrix}
A_1^1 & A_2^1 & A_3^1 & 0 & 0 & 0 & \cdots \\
0 & A_2^2 & A_3^2 & A_4^2 & 0 & 0 & \cdots \\
0 & 0 & A_3^3 & A_4^3 & A_5^3 & 0 & \cdots \\
\vdots & \vdots & \vdots & \vdots & \vdots & \vdots & \ddots
\end{pmatrix}
\tag{29}
$$

and

$$
A_{i+j-1}^i = \sum_{r=1}^{i} \overbrace{\mathbb{I}_{Q\times Q} \otimes \cdots \otimes \underset{\substack{\uparrow \\ r\text{th position}}}{F^{(j)}} \otimes \cdots \otimes \mathbb{I}_{Q\times Q}}^{i \text{ factors}}.
\tag{30}
$$

$\mathbb{I}_{Q\times Q}$ is the identity matrix; a proof is given in Forets and Pouly [47]. The truncated Carleman linearization simply terminates the series at degree k, neglecting all terms of degree $k+1$ and higher:

$$
C^{(k)} = \begin{pmatrix}
A_1^1 & A_2^1 & A_3^1 & 0 & 0 & \cdots & 0 & 0 & 0 & 0 \\
0 & A_2^2 & A_3^2 & A_4^2 & 0 & \cdots & 0 & 0 & 0 & 0 \\
\vdots & \vdots & \vdots & \vdots & \vdots & \ddots & \vdots & \vdots & \vdots & \vdots \\
0 & 0 & 0 & 0 & 0 & \cdots & 0 & A_{k-2}^{k-2} & A_{k-1}^{k-2} & A_k^{k-2} \\
0 & 0 & 0 & 0 & 0 & \cdots & 0 & 0 & A_{k-1}^{k-1} & A_k^{k-1} \\
0 & 0 & 0 & 0 & 0 & \cdots & 0 & 0 & 0 & A_k^k
\end{pmatrix}.
\tag{31}
$$

Carleman-linearized LBE on spatial discretization grids

To describe a spatially discretized system with n grid points, we introduce the following notation. Greek letters are used to index grid points (e.g., $\mathbf{x}_\alpha$, $\alpha \in 1, \ldots, n$), to prevent confusion with the (italic) indices of discrete velocities. In place of the single-point objects f, V, A, F, and C, we use ϕ, $\mathcal{V}$, $\mathcal{A}$, $\mathcal{F}$, and $\mathcal{C}$ to denote their n-point counterparts.

The distribution functions $f_m(\mathbf{x}_\alpha)$ at each grid point are arranged into an nQ-length vector

$$
\begin{aligned}
\phi(\mathbf{x}) &= (f(\mathbf{x_1}), \ldots, f(\mathbf{x_n}))^{\mathrm{T}} \\
&= (f_1(\mathbf{x}_1), \ldots, f_Q(\mathbf{x}_1), f_1(\mathbf{x}_2), \ldots, f_Q(\mathbf{x}_2), \ldots, f_1(\mathbf{x}_n), \ldots, f_Q(\mathbf{x}_n))^{\mathrm{T}}.
\end{aligned}
\tag{32}
$$

The k-forms $\phi^{[k]}(\mathbf{x})$, then, include both local and nonlocal terms, i.e., products of distribution functions at different positions. While the streaming operator S in Eq. (22), implemented as finite differences, connects distribution functions at different locations, the collision operator is purely local. Thus, the n-point versions of $F^{(1)}$, $F^{(2)}$, and $F^{(3)}$ are n-fold block repetitions of the single-point versions; define

$$
\mathcal{F}^{(i)}(\mathbf{x}_\alpha) = \delta_\alpha^{[i]} \otimes F^{(i)},
\tag{33}
$$

where the local nature of the collision operator is expressed by the vector

$$
\delta_\alpha = (\underbrace{0, \ldots, \overbrace{1}^{\alpha\text{th position}}, \ldots, 0}_{n \text{ elements}}).
\tag{34}
$$

Further define

$$
\mathcal{F}^{(i)}(\mathbf{x}) = (\mathcal{F}^{(i)}(\mathbf{x}_1), \ldots, \mathcal{F}^{(i)}(\mathbf{x}_n)).
\tag{35}
$$

It follows from Eq. (33) that

$$
\mathcal{F}^{(i)}(\mathbf{x}_\alpha)[\underbrace{f(\mathbf{x}_\beta) \otimes \cdots \otimes f(\mathbf{x}_\gamma)}_{i \text{ factors}}] = F^{(i)} f^{[i]}(\mathbf{x}_\alpha) \delta_{\alpha\beta} \ldots \delta_{\alpha\gamma},
\tag{36}
$$

where $\delta_{\alpha\beta}$ is the Kronecker delta function. In other words, products of the form $\mathcal{F}^{(i)}(\mathbf{x})\phi^{[i]}(\mathbf{x})$ only involve operations

on individual grid points even though the $\mathcal{F}^{(i)}(\mathbf{x})$ matrices and $\phi(\mathbf{x})$ vector span all n grid points. We will refer to this property as diagonality in $\mathbf{x}$.

Analogous to Eq. (22), the n-point LBE is

$$\frac{\partial \phi(\mathbf{x})}{\partial t} = -S\phi(\mathbf{x}) + \mathcal{F}^{(1)}(\mathbf{x})\phi(\mathbf{x}) + \mathcal{F}^{(2)}(\mathbf{x})\phi^{[2]}(\mathbf{x}) + \mathcal{F}^{(3)}(\mathbf{x})\phi^{[3]}(\mathbf{x}). \tag{37}$$

The n-point Carleman matrix involves n-point versions of the transfer matrices A^i_j; these are obtained by inserting Eq. (35) into the n-point equivalent of Eq. (30):

$$\mathcal{A}^i_{i+j-1}(\mathbf{x}) = \sum_{r=1}^i \overbrace{\mathbb{I}_{nQ \times nQ} \otimes \cdots \otimes \underset{\underset{r\text{th position}}{\uparrow}}{\mathcal{F}^{(j)}(\mathbf{x})} \otimes \cdots \otimes \mathbb{I}_{nQ \times nQ}}^{i \text{ factors}}. \tag{38}$$

It follows from Eq. (36) that

$$\mathcal{A}^i_{i+j-1}(\mathbf{x}_\alpha)[\underbrace{f(\mathbf{x}_\beta) \otimes \cdots \otimes f(\mathbf{x}_\gamma)}_{i+j-1 \text{ factors}}] = A^i_{i+j-1} f^{[i]}(\mathbf{x}_\alpha)\delta_{\alpha\beta}\ldots\delta_{\alpha\gamma}. \tag{39}$$

Thus, $\mathcal{A}^i_{i+j-1}(\mathbf{x}_\alpha)$ is also diagonal in $\mathbf{x}$.

The streaming operator can be implemented as finite differences between neighboring points (not necessarily restricted to nearest neighbors if better than second-order accuracy is desired, but $O(Q)$ for any reasonable finite difference implementation). This results in a matrix form for S with $O(Q)$ off-diagonal bands, and transfer matrices that are obtained from Eq. (38) by inserting S instead of $\mathcal{F}^{(1)}$. We denote these transfer matrices of S as $\mathcal{B}^i_i$; since $S\phi(\mathbf{x})$ is linear in $\phi(\mathbf{x})$, $\mathcal{B}$ only enters on the block diagonal of $\mathcal{C}(\mathbf{x})$. (Note that, while $\mathcal{B}$ is diagonal in Carleman degree, it is not diagonal in $\mathbf{x}$.)

The sum of the streaming Carleman matrix

$$\mathcal{C}^{(k)}_s(\mathbf{x}) = -\begin{pmatrix} \mathcal{B}^1_1 & 0 & 0 & 0 & 0 & \ldots & 0 & 0 & 0 & 0 \\ 0 & \mathcal{B}^2_2 & 0 & 0 & 0 & \ldots & 0 & 0 & 0 & 0 \\ \vdots & \vdots & \vdots & \vdots & \vdots & \ddots & \vdots & \vdots & & \vdots & \vdots \\ 0 & 0 & 0 & 0 & 0 & \ldots & 0 & \mathcal{B}^{k-2}_{k-2} & 0 & 0 \\ 0 & 0 & 0 & 0 & 0 & \ldots & 0 & 0 & \mathcal{B}^{k-1}_{k-1} & 0 \\ 0 & 0 & 0 & 0 & 0 & \ldots & 0 & 0 & 0 & \mathcal{B}^k_k \end{pmatrix} \tag{40}$$

and the collision-term n-point Carleman matrix

$$\mathcal{C}^{(k)}_c(\mathbf{x}) = \begin{pmatrix} \mathcal{A}^1_1(\mathbf{x}) & \mathcal{A}^1_2(\mathbf{x}) & \mathcal{A}^1_3(\mathbf{x}) & 0 & 0 & \ldots & 0 & 0 & 0 & 0 \\ 0 & \mathcal{A}^2_2(\mathbf{x}) & \mathcal{A}^2_3(\mathbf{x}) & \mathcal{A}^2_4(\mathbf{x}) & 0 & \ldots & 0 & 0 & 0 & 0 \\ \vdots & \vdots & \vdots & \vdots & \vdots & \ddots & \vdots & \vdots & & \vdots \\ 0 & 0 & 0 & 0 & 0 & \ldots & 0 & \mathcal{A}^{k-2}_{k-2}(\mathbf{x}) & \mathcal{A}^{k-2}_{k-1}(\mathbf{x}) & \mathcal{A}^{k-2}_k(\mathbf{x}) \\ 0 & 0 & 0 & 0 & 0 & \ldots & 0 & 0 & \mathcal{A}^{k-1}_{k-1}(\mathbf{x}) & \mathcal{A}^{k-1}_k(\mathbf{x}) \\ 0 & 0 & 0 & 0 & 0 & \ldots & 0 & 0 & 0 & \mathcal{A}^k_k(\mathbf{x}) \end{pmatrix} \tag{41}$$

then yields the n-point truncated Carleman matrix at degree k:

$$\mathcal{C}^{(k)}(\mathbf{x}) = \mathcal{C}^{(k)}_s(\mathbf{x}) + \mathcal{C}^{(k)}_c(\mathbf{x}). \tag{42}$$

Similarly, the n-point Carleman vector becomes

$$\mathcal{V}^{(k)}(\mathbf{x}) = (\phi(\mathbf{x}), \phi^{[2]}(\mathbf{x}), \ldots, \phi^{[k]}(\mathbf{x}))^\mathrm{T}, \tag{43}$$

leading to the Carleman-linearized truncated LBE over n grid points:

$$\frac{\partial \mathcal{V}^{(k)}(\mathbf{x})}{\partial t} = \mathcal{C}^{(k)}(\mathbf{x})\mathcal{V}^{(k)}(\mathbf{x}), \tag{44}$$

which, like the single-point Carleman LBE, is a system of linear differential equations in matrix form. In contrast to the single-point Carleman vector $V^{(k)}$, which has dimension $\sum_{i=1}^{k} Q^i$, the dimension of the n-point Carleman vector $\mathcal{V}^{(k)}(\mathbf{x})$ is $\sum_{i=1}^{k} n^i Q^i$. Note that $\mathcal{C}_c^{(k)}(\mathbf{x})$, all its transfer-matrix blocks being diagonal in $\mathbf{x}$ by Eq. (39), is also diagonal in $\mathbf{x}$, a property we will use extensively in the quantum-algorithm complexity analysis.

The first problem that we would like to solve involves assuming that we are given an initial distribution $\phi(0)$ that is efficiently computable over our lattice, an evolution time t and an error tolerance ϵ_{dyn} to generate a quantum state $|\mathcal{V}^{(k)}(x,t)\rangle$ such that $\| |\mathcal{V}^{(k)}(x,t)\rangle - \mathcal{V}^{(k)}(x,t)/\|\mathcal{V}^{(k)}(x,t)\| \| \leq \epsilon_{\text{dyn}}$.

The problem is the natural problem to first look at, however, it ignores the fact that the observables we are interested in do not act on the extended Hilbert space invoked through the use of Carleman linearization. The overall problem that we are interested in is then if we define the projector onto the first Carleman block to be $|\phi_0\rangle\langle\phi_0| \otimes I$ then we aim to minimize

$$\|(\langle\phi_0| \otimes I)(|\mathcal{V}^{(k)}(x,t)\rangle)/\|(\langle\phi_0| \otimes I)(|\mathcal{V}^{(k)}(x,t)\rangle\| - \phi(x)/\|\phi(x)\|\| \leq \epsilon_{\text{total}}. \tag{45}$$

Our aim is then to separate the two sources of error in the problem and use to observation that if $\epsilon_{\text{total}} \leq \epsilon_{\text{dyn}} + \epsilon_{\text{carl}}$ then it suffices to make both of these error sources small. Through existing arguments, we can construct a quantum algorithm that makes the former small. We will make arguments here based on perturbation theory backed by numerics that ϵ_{carl} can be made small in regimes of practical interest using small values of k.

RESULTS

Carleman truncation error

We now analyze the effect of truncating the infinite-dimensional Carleman system of equations at a finite degree. We show that the zeroth and first moments of the lattice Boltzmann distribution functions (ρ and $\rho\mathbf{u}$) at kth degree receive corrections from the higher-order Carleman variables at degrees $k+1$ and $k+2$ and that these corrections are suppressed by $O(\text{Ma}^2)$.

The macroscopic properties of the LBE fluid are given by moments of the lattice Boltzmann distribution functions, as can be seen from Eq. (15)–(16): the zeroth moment gives ρ, and the first moment gives $\rho\mathbf{u}$. We introduce the coefficient vectors

$$\Phi_\rho = (1, \ldots, 1) \tag{46}$$

and

$$\Phi_{\rho u} = (\mathbf{e}_1, \ldots, \mathbf{e}_Q), \tag{47}$$

which recover the macroscopic fluid variables by matrix-multiplying the vector of distribution functions such that

$$\rho = \sum_m (\Phi_\rho)_m f_m = \Phi_\rho f \tag{48}$$

and

$$\rho\mathbf{u} = \sum_m (\Phi_{\rho u})_m f_m = \Phi_{\rho u} f. \tag{49}$$

From the mixed-product property of the Kronecker product,

$$(A \otimes B)(C \otimes D) = (AC) \otimes (BD), \tag{50}$$

it follows that

$$(\rho)^p (\rho\mathbf{u})^q = (\Phi_\rho f)^{[p]} (\Phi_{\rho u} f)^{[q]}$$
$$= \left(\Phi_\rho^{[p]} \otimes \Phi_{\rho u}^{[q]}\right) f^{[p+q]} \tag{51}$$

for arbitrary integers p and q (where products of spatial vectors imply the dot product).

Furthermore, inserting the quadratic and cubic terms in Eq. (20), we obtain (introducing the shorthand notation ζ_2 and ζ_3):

$$\Phi_\rho F^{(2)} f^{[2]} = \frac{2}{\mathrm{Kn}\tau} \sum_m w_m \left[c(\mathbf{e}_m \cdot \rho\mathbf{u})^2 + d\rho^2 u^2 \right] = \zeta_2 \rho^2$$

$$= O((\mathrm{Kn}\tau)^{-1} \rho^2 u^2) \tag{52}$$

$$\Phi_\rho F^{(3)} f^{[3]} = -\frac{1}{\mathrm{Kn}\tau} \sum_m w_m \left[c\rho^3 (\mathbf{e}_m \cdot \mathbf{u})^2 + d\rho^3 u^2 \right] = \zeta_3 \rho^3$$

$$= O((\mathrm{Kn}\tau)^{-1} \rho^3 u^2) \tag{53}$$

$$\tag{54}$$

$$\Phi_{\rho u} F^{(2)} f^{[2]} = \frac{2}{\mathrm{Kn}\tau} \sum_m w_m \mathbf{e}_m \left[c(\mathbf{e}_m \cdot \rho\mathbf{u})^2 + d\rho^2 u^2 \right] = 0 \tag{55}$$

$$\Phi_{\rho u} F^{(3)} f^{[3]} = -\frac{1}{\mathrm{Kn}\tau} \sum_m w_m \mathbf{e}_m \left[c\rho^3 (\mathbf{e}_m \cdot \mathbf{u})^2 + d\rho^3 u^2 \right] = 0, \tag{56}$$

where the result $\Phi_{\rho u} F^{(2)} f^{[2]} = \Phi_{\rho u} F^{(3)} f^{[3]} = 0$ is a consequence of lattice symmetry dictating that the nonresting particles occur in pairs of equal weight w_m but opposite direction $\mathbf{e}_m$, and the bounds in Eq. (52) and Eq. (53) stem from $w_m = O(1)$ and $\sum_m w_m = 1$.

The lowest-order correction to $\partial V^{(k)}/\partial t$ is given by the elements of $C^{(k+1)}$ that are not present in $C^{(k)}$. At this point, for concreteness, we consider $k = 3$ as an example:

$$\left[\frac{\partial f^{[2]}}{\partial t} \right]'_{(4)} = A_4^2 f^{[4]} \tag{57}$$

$$\left[\frac{\partial f^{[3]}}{\partial t} \right]'_{(4)} = A_4^3 f^{[4]}, \tag{58}$$

where $[\partial/\partial t]'_{(k+1)}$ denotes said correction. By the definition of A^i_{i+j-1} (Eq. (30)),

$$A_4^2 = F^{(3)} \otimes \mathbb{I}_{Q \times Q} + \mathbb{I}_{Q \times Q} \otimes F^{(3)} \tag{59}$$

$$A_4^3 = F^{(2)} \otimes \mathbb{I}_{Q \times Q} \otimes \mathbb{I}_{Q \times Q} + \mathbb{I}_{Q \times Q} \otimes F^{(2)} \otimes \mathbb{I}_{Q \times Q} + \mathbb{I}_{Q \times Q} \otimes \mathbb{I}_{Q \times Q} \otimes F^{(2)}. \tag{60}$$

Using Φ_ρ and $\Phi_{\rho u}$ to construct corrections to degree 2 and 3 polynomials of ρ and $\rho\mathbf{u}$ yields, again by the mixed-product rule (Eq. (50)), substituting the expressions from Eq. (20) for $F^{(2)} f^{[2]}$ and $F^{(3)} f^{[3]}$, and making use of Eq. (52)–(56):

$$\left[\frac{\partial \rho^2}{\partial t} \right]'_{(4)} = \Phi_\rho^{[2]} \left[\frac{\partial f^{[2]}}{\partial t} \right]'_{(4)} = \Phi_\rho^{[2]} A_4^2 f^{[4]}$$

$$= (\Phi_\rho \otimes \Phi_\rho) \left(F^{(3)} \otimes \mathbb{I}_{Q \times Q} + \mathbb{I}_{Q \times Q} \otimes F^{(3)} \right) (f \otimes f \otimes f \otimes f)$$

$$= (\Phi_\rho F^{(3)} f^{[3]}) \otimes (\Phi_\rho \mathbb{I}_{Q \times Q} f) + (\Phi_\rho \mathbb{I}_{Q \times Q} f) \otimes (\Phi_\rho F^{(3)} f^{[3]})$$

$$= -\frac{2}{\mathrm{Kn}\tau} d u^2 \rho \tag{61}$$

$$\left[\frac{\partial \rho^2 u^2}{\partial t} \right]'_{(4)} = \Phi_{\rho u}^{[2]} \left[\frac{\partial f^{[2]}}{\partial t} \right]'_{(4)} = \Phi_{\rho u}^{[2]} A_4^2 f^{[4]}$$

$$= (\Phi_{\rho u} \otimes \Phi_{\rho u}) \left(F^{(3)} \otimes \mathbb{I}_{Q \times Q} + \mathbb{I}_{Q \times Q} \otimes F^{(3)} \right) (f \otimes f \otimes f \otimes f)$$

$$= 0. \tag{62}$$

We now derive a recursion formula for the higher-order corrections to powers of ρ and $\rho\mathbf{u}$ at arbitrary order, following steps very similar to the $k = 3$ example. At any Carleman order k, corrections to $f^{[k-1]}$ and $f^{[k]}$ arise due

to the neglected terms containing $f^{[k+1]}$, which, by inspection of Eq. (31), can be written as

$$\left[\frac{\partial f^{[k-1]}}{\partial t}\right]'_{(k+1)} = A^{k-1}_{k+1}f^{[k+1]} \tag{63}$$

$$\left[\frac{\partial f^{[k]}}{\partial t}\right]'_{(k+1)} = A^{k}_{k+1}f^{[k+1]}. \tag{64}$$

These equations are analogous to Eq. (57)–(58) for the $k = 3$ example. Only these two subvectors of V receive corrections due to the diagonal band structure of Eq. (29), whose striping is determined by the presence of terms up to cubic degree in Eq. (22). The corresponding corrections to powers of the macroscopic fluid variables can be derived by left multiplication with Kronecker powers of Φ_ρ and $\Phi_{\rho u}$ in analogy to Eq. (61)–(62):

$$\left[\frac{\partial \rho^{k-1}}{\partial t}\right]'_{(k+1)} = \Phi^{[k-1]}_\rho A^{k-1}_{k+1}f^{[k+1]}$$

$$= \left(\Phi^{[k-2]}_\rho \otimes \Phi_\rho\right)\left[\sum_{r=1}^{k-1}\mathbb{I}^{[r-1]}_{Q\times Q} \otimes F^{(3)} \otimes \mathbb{I}^{[k-r-1]}_{Q\times Q}\right]\left(f^{[k-2]} \otimes f^{[3]}\right)$$

$$= -\frac{k-1}{\text{Kn}\tau}\left(\sum_m w_m\left[c\rho^3(\mathbf{e}_m\cdot\mathbf{u})^2 + d\rho^3 u^2\right]\right)\rho^{k-2}$$

$$= O(k(\text{Kn}\tau)^{-1}\rho^{k+1}u^2) \tag{65}$$

$$\left[\frac{\partial \rho^k}{\partial t}\right]'_{(k+1)} = \Phi^{[k]}_\rho A^{k}_{k+1}f^{[k+1]}$$

$$= \left(\Phi^{[k-1]}_\rho \otimes \Phi_\rho\right)\left[\sum_{r=1}^{k}\mathbb{I}^{[r-1]}_{Q\times Q} \otimes F^{(2)} \otimes \mathbb{I}^{[k-r]}_{Q\times Q}\right]\left(f^{[k-1]} \otimes f^{[2]}\right)$$

$$= \frac{2k}{\text{Kn}\tau}\left(\sum_m w_m\left[c\rho^2(\mathbf{e}_m\cdot\mathbf{u})^2 + d\rho^2 u^2\right]\right)\rho^{k-1}$$

$$= O(k(\text{Kn}\tau)^{-1}\rho^{k+1}u^2) \tag{66}$$

$$\left[\frac{\partial \rho^p u^q}{\partial t}\right]'_{(k+1)} = 0, \quad p \geq 0, q > 0, p+q = k-1 \tag{67}$$

$$\left[\frac{\partial \rho^p u^q}{\partial t}\right]'_{(k+1)} = 0, \quad p \geq 0, q > 0, p+q = k, \tag{68}$$

for integer p and q, where Eq. (67) and Eq. (68) follow from Eq. (55) and Eq. (56). Thus, the macroscopic fluid properties follow a hierarchy where subsequent higher-order corrections are suppressed by factors of $O(u^2) = O(\text{Ma}^2)$ relative to the highest-order retained terms. Since the LBE is restricted to $\text{Ma} \ll 1$, the Carleman truncation error and the Taylor expansion error on $1/\rho$ are small even when a low Carleman truncation order is used. We also note that the expression for the truncation error is independent of the system size and Reynolds number, since the overall $(\text{Kn}\tau)^{-1}$ normalization is common to the retained and neglected terms.

As a numerical consistency check of the Carleman-linearized nonlinear collision term of Eq. (7), we perform the LBM and the Carleman-linearized LBM numerical experiments. We choose the two-dimensional Taylor–Green (TG) flow because it is an analytical solution [49] of the NSE and can serve as a benchmark for validating the simulation results. The simulations are initialized with a given TG initial velocity U_0. The periodic boundary condition is adopted. To check the Ma dependency of the relative error, we perform simulations for different initial Ma with the same initial Re. This is achieved by varying ν and initial velocity while keeping n the same. The relative error of the maximum u_x (x component of the simulated velocity of the TG flow) of LBM with the Carleman-linearized collision term compared to LBM is shown in Figure 2. We first observe that the relative error is small ($O(10^{-10})$) (Figure 2), showing that the Carleman-linearized LBM can accurately reproduce the LBM over the range considered. At a given time, the relative error increases with increasing initial Ma, which is consistent with our finding that the Carleman truncation error scales with Ma.
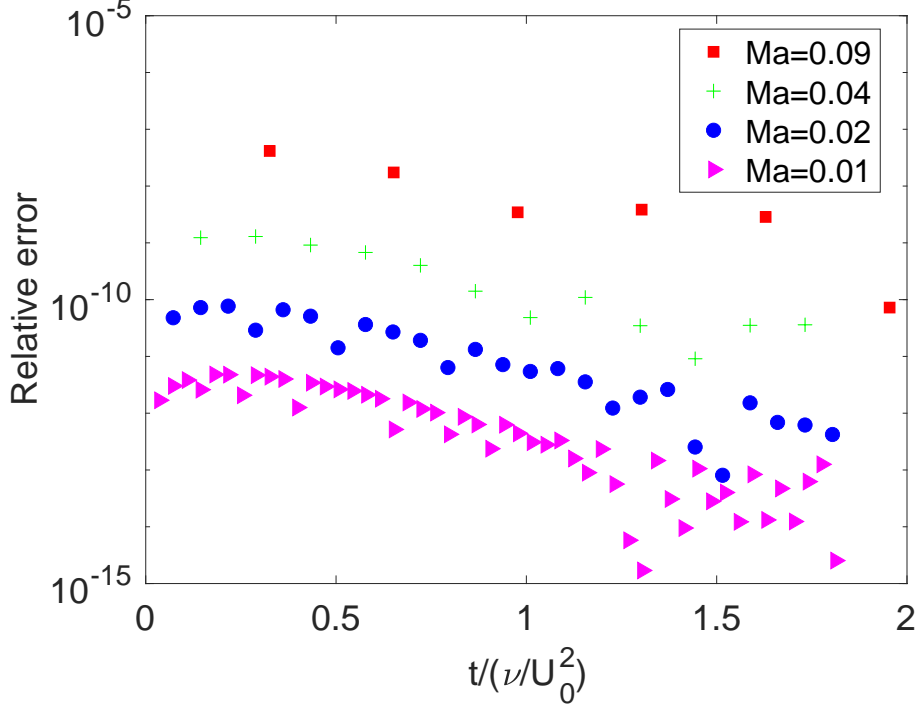
FIG. 2. Relative error of the maximum u_x between Carleman-linearized LBM and LBM simulations for different initial Ma (Ma = 0.01, 0.02, 0.04, 0.09 are represented by magenta triangles, blue dots, green pluses, and red squares, respectively) at fixed initial Re = 100. The x-axis represents the simulation time t normalised by the kinetic diffusion time scale ν/U_0^2, i.e., kinetic viscosity divided by square of the initial flow velocity.

Quantum algorithm complexity

In this section, we derive bounds on the complexity of applying the Berry *et al.* [39] algorithm to the Carleman-linearized LBE of degree 3 at n spatial grid points with Q discrete velocities (Eq. (44)). For notational compactness, we introduce the abbreviated notation

$$\mathcal{V} = \mathcal{V}^{(3)}(\mathbf{x}) \tag{69}$$

$$\mathcal{C} = \mathcal{C}^{(3)}(\mathbf{x}). \tag{70}$$

Carleman order $k = 3$ is explicitly chosen as we showed above that the truncation error at $k = 3$ is $O(\mathrm{Ma}^2)$, which is sufficient to prevent truncation error from dominating the solution error.

Properties of the physical system

Before proceeding further, we summarize the properties of the physical systems which can be simulated using our procedure, including conditions that the systems must satisfy for the procedure to be applicable. We also give typical values of system parameters for a particular application (atmospheric turbulence). The key unrestricted parameter of the physical application is the number of grid points n. For simulations of turbulent flows, the $n \gg 1$ behavior of the algorithm is of utmost interest; for example, for direct simulations of atmospheric turbulence, $n > 10^{20}$ is desirable (and unattainable using state-of-the-art algorithms on classical computers).

a.   *Parameters of restricted range*   The fluid flow to be modeled by our procedure needs to satisfy certain conditions. These conditions restrict two parameters of the flow, the Mach number Ma and Knudsen number Kn. First, the flow needs to be "weakly compressible", i.e., Ma $\ll$ 1. This is a requirement both for the LBE to recover the NSE and for the linearized LBE to approximate the nonlinear LBE (both of which errors scale as Ma^2). In LBM practice,

Ma $< 10^{-1}$ is a typical upper bound, but atmospheric flow satisfies Ma $\leq 10^{-2}$ in most circumstances. Second, the flow to be modeled must also be "continuum flow", i.e., macroscopic features like turbulent eddies must be much larger than the molecular scale. This is reflected in Boltzmann relaxation parameter Kn$\tau \ll 1$. Typical values in the atmosphere are Kn $< 10^{-8}$. The scaled relaxation τ is restricted to the range $0.5 < \tau \leq 1$ in LBM practice. Furthermore, the relaxation parameter restricts the number of grid points according to Eq. (93) to $\log n \ll (\text{Kn}\tau)^{-3}$. This restriction is unlikely to have practical consequences; in the atmospheric example, it is equivalent to $n \ll \exp(10^{24})$. For atmospheric flow, Ma $\ll 1$ is the most restrictive condition.

    b.   Free parameters   The number of spatial grid points n used to resolve the flow is unrestricted, i.e., application science would like the largest value possible subject to getting a result within a reasonable wallclock time limit. Reynolds number Re is similarly unrestricted, i.e., application science would like the largest value possible. Typical values of these parameters currently attainable using state-of-the-art classical algorithms and computers are $n \approx 10^9$ and Re $\approx 10^5$. The parameters Re, n, and physical integral domain size L are not independent; higher Re requires finer resolution, implying higher n/L^d (in d spatial dimensions). A transformational capability in atmospheric science would be direct numerical simulation of entire cloud systems ($L \approx 100$ km) at Re $\approx 10^9$, which requires a spatial grid spacing of 1 mm (Kolmogorov length scale) or $n \approx 10^{21}$.

    The physical integration time $\tilde{T}$ depends on specifics of the physical problem. It is typically determined by the time required for the turbulence to spin up from homogeneous initial conditions and for the turbulent eddies then to turn over several times so that domain-mean statistics are representative of the fully developed turbulent steady state.

    c.   Constants   The number of discrete molecular velocities Q is fixed, i.e., the same value can be used for simulation of arbitrary systems (as long as Ma $\ll 1$); values in widespread use are $Q \in \{3, 9, 27\}$ for 1D, 2D, and 3D fluid flows, respectively. The constants $a = 1$, $b = 3$, $c = 9/2$, $d = -3/2$ are fixed for all lattice geometries, and the w_m are fixed for each specific lattice geometry. For this reason, we consider these parameters to be constants; however, for some simulations it may be appropriate to take these to be free parameters that change as the desired simulation accuracy increases to minimize algorithmic complexity.

    d.   Solution error sources   Two distinct sources of solution error appear. The first is due to the Carleman-linearized LBE being an approximation to the actual NSE dynamics of the system; this error is $O(\text{Ma}^2)$, hence the Ma $\ll 1$ requirement for our procedure to be applicable. The second is discretization error in the time integration of $\partial \mathcal{V}/\partial t = \mathcal{C}\mathcal{V}$ in the quantum algorithm; this is parameterized by ϵ, which should be chosen so it is not the dominant error, i.e., $\epsilon = O(\text{Ma}^2)$.

Contributions to algorithm complexity

    The complexity of solving Eq. (44) is given by Eq. (3) in terms of the properties of the coefficient matrix $\mathcal{C}$ and the solution vector $\mathcal{V}$; for ease of reference, the equation is reproduced here:

$$\text{gate complexity} = O(\|\mathcal{C}\|\kappa_J g T s \cdot \text{poly}(\log{(\kappa_J s g \beta T \|\mathcal{C}\| N/\epsilon)})), \tag{3}$$

where $\mathcal{C} = \mathcal{J}\mathcal{D}\mathcal{J}^{-1}$ is an $N \times N$ diagonalizable matrix with eigenvalues $\mathcal{D} = \text{diag}(\lambda_i)$ ($i \in 1, \ldots, N$) whose real part $\mathcal{R}(\lambda_i) \leq 0 \ \forall i$. The norm $\|\mathcal{C}\|$ is the 2-norm, the largest singular value of $\mathcal{C}$. Here we consider the gate complexity to be the number of one and two-qubit gates needed for the simulation. The condition number in the above expression,

$$\kappa_{\mathcal{J}} = \|\mathcal{J}\| \cdot \|\mathcal{J}^{-1}\|, \tag{71}$$

is the condition number of the matrix $\mathcal{J}$ of eigenvectors of $\mathcal{C}$. The dissipation parameter g is defined as

$$g = \max_{t \in [0,T]} \|\mathcal{V}(t)\|/\|\mathcal{V}(T)\|, \tag{72}$$

with T the evolution time, and s is the sparsity (number of nonzero entries per row) of $\mathcal{C}$. The initial condition norm enters through

$$\beta = (\|\,|\mathcal{V}_{\text{in}}\rangle\|)/\|\,|\mathcal{V}(T)\rangle\| = O(1), \tag{73}$$

which is dependent on the physical problem under consideration but independent of other system parameters. The number of degrees of freedom N, which is the dimension of $\mathcal{C}$ and $\mathcal{V}$, is given in terms of the number of grid points n and discrete velocities Q by

$$N = (n^3 Q^3 + n^2 Q^2 + nQ). \tag{74}$$

The term-by-term analysis of the factors that determine the algorithm's complexity (Eq. (3)) is conducted below.

e. Sparsity The coefficient matrices $F^{(1)}$, $F^{(2)}$, and $F^{(3)}$ and resulting transfer matrices A_j^i for a single point contain $O(Q^3 \times Q^3)$ elements. In the n-point Carleman matrix, locality is enforced by Eq. (33), so that the nonzero elements of the collision Carleman matrix (Eq. (41)) are diagonal in $\mathbf{x}$.

The streaming operator S involves the $O(Q)$ nearest (or potentially next-to-nearest, next-to-next-to-nearest, etc., if higher-order accuracy for the gradient operator is desired) neighbors in space. This results in bands in S that are not diagonal in $\mathbf{x}$, yielding an additional $O(Q^3 \times Q^3)$ off-diagonal elements in the streaming Carleman matrix, i.e., the first term in Eq. (42).

The sparsity, i.e., the total number of nonzero elements in each row of $\mathcal{C}$, is bounded by the sum of the sparsity of the collision Carleman matrix and the sparsity of the streaming Carleman matrix, both of which are $O(Q^3)$; thus,

$$s = O(1), \tag{75}$$

i.e, sparsity is independent of the number of grid points n and other free parameters of the system for the fixed discretization schemes considered here.

f. Matrix norm We now determine the norm of the Carleman matrix $\mathcal{C}$ (Eq. (42)). The matrix 2-norm of a matrix M is bounded by its 1-norm and its ∞-norm:

$$\|M\| \leq \sqrt{\|M\|_1 \|M\|_\infty}. \tag{76}$$

The 1-norm and ∞-norm of $\mathcal{C}$ can both be directly bounded, since they equal the maximum absolute column sum and maximum absolute row sum of the matrix, respectively. By Eq. (75), there are $O(Q^3)$ nonzero elements in each row. From Eq. (20), these elements are each $O((\mathrm{Kn}\tau)^{-1})$, so that $\|\mathcal{C}\|_\infty = O(Q^3(\mathrm{Kn}\tau)^{-1})$. We note that Eq. (75) also gives the number of nonzero elements in each column due to the diagonality of $\mathcal{C}$ in $\mathbf{x}$, so that $\|\mathcal{C}\|_1$ has the same scaling as $\|\mathcal{C}\|_\infty$. Therefore, the overall scaling of the matrix norm with the free parameters of the system is

$$\|\mathcal{C}\| = O((\mathrm{Kn}\tau)^{-1}). \tag{77}$$

In practice, $\tau = O(1)$, because $\tau > 0.5$ is required for the stability of the LBM [50]. Thus we have

$$\|\mathcal{C}\| = O(\mathrm{Kn}^{-1}). \tag{78}$$

g. Condition number To bound $\kappa_\mathcal{J}$, we need to find the eigenvectors of $\mathcal{C}$. This is not possible analytically for arbitrary n; if an analytic expression for the eigenvectors could be obtained, a quantum algorithm, or any numerical simulation, would no longer be required to calculate the dynamics of the system described by $\mathcal{C}$. We will derive a bound on $\kappa_\mathcal{J}$ in three steps. First, we will numerically diagonalize the single-point collision Carleman matrix C at Carleman order $k = 3$ (Eq. (31)) for lattice structures used to recover the NSE from the LBE; these are specific matrices with fixed, explicitly known a, b, c, d, w_m, and Q parameters in Eq. (20), but they can solve general flows [35]. Second, we will show that the eigenvectors of the n-point collision Carleman matrix $\mathcal{C}_c(\mathbf{x})$, defined in Eq. (41), can be constructed from the eigenvectors of the single-point C. Third, we will perform a perturbative expansion to include the effect of the streaming Carleman matrix $\mathcal{C}_s(\mathbf{x})$, defined in Eq. (40), and derive an approximate expression for $\kappa_\mathcal{J}$ that holds as long as the Knudsen number of the flow is small; this condition needs to be satisfied for the LBE to describe the flow. The numbered paragraphs below provide the details of these three steps.

1. In one, two, and three spatial dimensions, the D1Q3, D2Q9, and D3Q27 lattice topologies are frequently used and are known to recover the NSE in the Ma $\ll 1$ limit [35] on which the present work focuses. The single-point collision Carleman matrices C and their spectral decompositions $C = JDJ^{-1}$ are provided as a data supplement [51]. By inspection of these numerical results, all eigenvalues of C are $-(\mathrm{Kn}\tau)^{-1} \times \{0, 1, 2, 3\}$, that is, they are either degenerate or separated by gaps of $(\mathrm{Kn}\tau)^{-1}$, as shown by the histogram of the eigenvalue spectra $\mathcal{R}(\lambda)$ in Fig. 3. The eigenvector matrices J and J^{-1} are similarly constant for each choice of $Q \in \{3, 9, 27\}$. The corresponding condition numbers are $\kappa_J = 12.94$ for D1Q3, $\kappa_J = 85.66$ for D2Q9, and $\kappa_J = 2269$ for D3Q27. Bounds based on Eq. (76) are $\kappa_J \leq 62.41$ for D1Q3, $\kappa_J \leq 2252$ for D2Q9, and $\kappa_J \leq 1.152 \times 10^5$ for D3Q27; these bounds will be used to generalize to n grid points below.

2. Denote the eigenvectors of the single-point C as ξ_i, $i \in 1, \ldots, Q$, and decompose

$$\xi_i = (\xi_i^{(1)}, \xi_i^{(2)}, \xi_i^{(3)})^\mathrm{T} \tag{79}$$

according to whether its elements represent 1-, 2-, or 3-form elements (powers of f_m polynomials defined in Eq. (22)) of the single-point Carleman vectors V. Using the δ_α vector from Eq. (34), we can construct localized

eigenvectors $\Xi_i(\mathbf{x}_\alpha)$ of the n-point collision Carleman matrix (Eq. (41)):

$$\Xi_i(\mathbf{x}_\alpha) = (\delta_\alpha \otimes \xi_i^{(1)}, \delta_\alpha^{[2]} \otimes \xi_i^{(2)}, \delta_\alpha^{[3]} \otimes \xi_i^{(3)})^{\mathrm{T}}. \tag{80}$$

By Eq. (39), $\Xi_i(\mathbf{x}_\alpha)$ is an eigenvector of the n-point collision matrix $\mathcal{C}_c^{(3)}(\mathbf{x})$ for any $\alpha \in 1, \ldots, n$, as the diagonality of the n-point transfer matrices in $\mathbf{x}$ ensures that the nonzero blocks of $\mathcal{C}_c$ are aligned with the nonzero blocks of $\Xi_i(\mathbf{x}_\alpha)$. The eigenvectors of the n-point collision Carleman matrix $\mathcal{C}_c$ are therefore a simple blockwise repetition of the eigenvectors of the single-point C. Furthermore, it follows from Eq. (80) that

$$\Xi_i(\mathbf{x}_\alpha)^{\mathrm{T}}\Xi_j(\mathbf{x}_\beta) = \xi_i^{\mathrm{T}}\xi_j\delta_{\alpha\beta}, \tag{81}$$

i.e., the eigenvectors at different grid points are mutually orthogonal. The corresponding eigenvalues are equal for all $\alpha \in 1, \ldots, n$, i.e., they are repetitions of the eigenvalues of C.

The $\Xi_i(\mathbf{x}_\alpha)$ are stacked column-wise or row-wise to form the eigenvector matrices of $\mathcal{C}_c$. Denote these eigenvector matrices as $\mathcal{J}_0$ and $\mathcal{J}_0^{-1}$. (The subscript 0 notation is used in anticipation of the perturbation analysis carried out in the next paragraph.) By Eq. (81), the eigenvectors localized at different grid points form blocks in $\mathcal{J}_0$ and $\mathcal{J}_0^{-1}$ that ensure that row and column sums on $\mathcal{J}_0$ and $\mathcal{J}_0^{-1}$ consist of the same $O(Q^3)$ nonzero elements as row and column sums on the *single-point constant* eigenvector matrices J and J^{-1}, rather than the full $O(n^3Q^3)$ dimension of the n-point matrices. Thus, the same spectral-norm bound from Eq. (76) applies to $\|J\|$ and $\|\mathcal{J}_0\|$; and the same bound applies to $\|J^{-1}\|$ and $\|\mathcal{J}_0^{-1}\|$. Thus, $\kappa_{\mathcal{J}_0}$ is fixed (for fixed Q), independent of n.

3. Finally, we bound the effect of the streaming contribution $\mathcal{C}_s$ to the eigenvectors of $\mathcal{C} = \mathcal{C}_s + \mathcal{C}_c$ and thence the effect on $\mathcal{J}$, $\mathcal{J}^{-1}$, and $\kappa_{\mathcal{J}}$. Inspection of Eq. (20) shows that the streaming term in the LBE is suppressed by $\mathrm{Kn} \ll 1$ relative to the collision term; this suggests that we can treat streaming using well established principles of (degenerate) perturbation theory [52], with the collision Carleman matrix in Eq. (42) constituting the base matrix (with known eigenvectors) and the streaming term constituting the $O(\mathrm{Kn}) \ll 1$ perturbation.

Item 2. above derived the properties of the n-point collision eigenvector matrices $\mathcal{J}_0$ and $\mathcal{J}_0^{-1}$ in terms of the single-point eigenvector matrices J and J^{-1} that had to be computed numerically. When the perturbation due to $\mathcal{C}_s$ is included, the eigenvectors are perturbed [52] in proportion to the perturbation strength $(\mathrm{Kn}\tau)$ and the gap size of the eigenvalue spectrum of $\mathcal{C}_c$, neglecting until the next paragraph the issue of degenerate eigenvalues. For notational convenience, we suppress the $\mathbf{x}_a$ notation on the eigenvectors of $\mathcal{C}_c$; the perturbed eigenvectors to first order are then given by $\Xi_i + \Xi_i'$, where

$$\Xi_i' = \mathrm{Kn}\tau \sum_{k \neq i} \frac{\Xi_i^{\mathrm{T}}\mathcal{C}_s\Xi_k}{\lambda_i - \lambda_k}\Xi_k. \tag{82}$$

Numerical calculation of the eigenvalue spectrum of the single-point Carleman matrices in item 1. above showed the gap between nondegenerate eigenvalues to be integer multiples of $(\mathrm{Kn}\tau)^{-1} \gg 1$, so the perturbation to the eigenvectors is proportional to $O((\mathrm{Kn}\tau)^2) \ll 1$ times the expectation values $\sum \Xi_i^{\mathrm{T}}\mathcal{C}_s\Xi_k$. In the nondegenerate case, the eigenvectors form an orthonormal basis, and the vector norm of the Ξ_i' can be bounded as follows:

$$\begin{aligned}
|\Xi_i'|^2 &= (\mathrm{Kn}\tau)^2 \sum_{k \neq i} \frac{\Xi_i^{\mathrm{T}}\mathcal{C}_s\Xi_k\Xi_k^{\mathrm{T}}\mathcal{C}_s^{\dagger}\Xi_i}{(\lambda_k - \lambda_i)^2} \\
&\leq \frac{(\mathrm{Kn}\tau)^2}{\min_k(\lambda_k - \lambda_i)^2} \sum_{k \neq i} \Xi_i^{\mathrm{T}}\mathcal{C}_s\Xi_k\Xi_k^{\mathrm{T}}\mathcal{C}_s^{\dagger}\Xi_i \\
&\leq \frac{(\mathrm{Kn}\tau)^2}{\min_k(\lambda_k - \lambda_i)^2} \left[\sum_k \Xi_i^{\mathrm{T}}\mathcal{C}_s\Xi_k\Xi_k^{\mathrm{T}}\mathcal{C}_s^{\dagger}\Xi_i - \left|\Xi_i^{\mathrm{T}}\mathcal{C}_s\Xi_i\right|^2 \right].
\end{aligned} \tag{83}$$

Using completeness and noting that the final term in Eq. (83) is nonpositive-definite,

$$|\Xi_i'|^2 \leq \frac{(\mathrm{Kn}\tau)^2}{\min_k(\lambda_k - \lambda_i)^2}\Xi_i^{\mathrm{T}}\mathcal{C}_s\mathcal{C}_s^{\dagger}\Xi_i, \tag{84}$$

and therefore

$$|\Xi'_i| \leq \frac{\text{Kn}\tau}{\min_k(\lambda_k - \lambda_i)}\|\mathcal{C}_s\|. \tag{85}$$

The eigenvalues of the streaming operator correspond to the spectrum of wavenumbers supported by the spatial discretization. On the lattice, these wavenumbers are rescaled according to Eq. (12) so that the maximum wavenumber is $O(1)$, and hence

$$|\Xi'_i| = O\left(\frac{\text{Kn}\tau}{\min_k(\lambda_k - \lambda_i)}\right). \tag{86}$$

As we determined numerically in Fig. 3, there are up to four (only three in the one-dimensional LBE) discrete eigenvalues $-\{0, 1, 2, 3\} \times (\text{Kn}\tau)^{-1}$, so

$$|\Xi'_i| = O((\text{Kn}\tau)^2). \tag{87}$$

The repetition of the single-point Carleman eigenvalues in the n-point Carleman eigenvalue spectrum means that each eigenvalue is highly degenerate. We therefore need to treat the case of eigenvalue degeneracy in Eq. (82). This, too, is a textbook application of perturbation theory [52]. The procedure treats each degenerate subspace of $\mathcal{J}_0$ and chooses the eigenbasis such that it diagonalizes the perturbation within each of the subspaces. There are up to four (only three in the one-dimensional LBE) such degenerate subspaces corresponding to the four discrete eigenvalues $-\{0, 1, 2, 3\} \times (\text{Kn}\tau)^{-1}$; we label these spaces D_0 through D_3. For each space, we define a projection operator

$$P_l = \sum_{\Xi_i \in D_l} \frac{\Xi_i \Xi_i^{\text{T}}}{\|\Xi_i\|^2}. \tag{88}$$

We then diagonalize the perturbation operator $\mathcal{C}_s$ in each degenerate subspace in turn. For the lth subspace, the first-order eigenvector perturbation is given by

$$P_l \Xi'_i = (\text{Kn}\tau)^2 P_l \sum_{j \neq i} \frac{\Xi_i}{\mu_j - \mu_i} \sum_{k \notin D_l} \Xi_i^{\text{T}} \mathcal{C}_s \Xi_k \frac{1}{\lambda_{D_l} - \lambda_k} \Xi_k^{\text{T}} \mathcal{C}_s \Xi_j \, , \tag{89}$$

where the projection operator ensures that the degeneracy-breaking diagonalization of $\mathcal{C}_s$ is only performed within each degenerate subspace and $\mu_{i,j}$ are the eigenvectors of $\mathcal{C}_s$; between subspaces, Eq. (82) continues to apply. The scaling of the terms in Eq. (89) is familiar except for $\sum(\mu_j - \mu_i)^{-1}$. This term needs careful examination because the smallest difference in eigenvalues of $\mathcal{C}_s$ is set by the smallest difference in scaled wavenumbers, which scales with the number of grid points as $n^{-1/D}$ in $D \in \{1, 2, 3\}$ spatial dimensions. In the $n \gg 1$ limit, we can bound this factor by

$$\sum_{j \neq i} \frac{1}{\mu_j - \mu_i} \propto \int_{\mathbf{k}_i \neq \mathbf{k}_j} \frac{d^D \mathbf{k}_j}{|\mathbf{k}_j - \mathbf{k}_i|} \propto \int_{k = O\left(n^{-\frac{1}{D}}\right)}^{O(1)} \frac{dk}{k} = O\left(\frac{1}{D}\log n\right). \tag{90}$$

Combining the various factors, the degenerate perturbations to Ξ_i are suppressed relative to the unperturbed eigenvectors (treating D as a fixed value rather than a parameter of the problem) by $O((\text{Kn}\tau)^3 \log n)$. The nondegenerate perturbations are suppressed by $O((\text{Kn}\tau)^2)$. The singular values of $\mathcal{J}$ are not necessarily smooth but can be evaluated from the eigenvalues of the square of $\mathcal{J}$, i.e., $\Sigma = \mathcal{J}^\dagger \mathcal{J}$. We then have that

$$\|\mathcal{J}^\dagger \mathcal{J} - \mathcal{J}_0^\dagger \mathcal{J}_0\| \leq (\|\mathcal{J}\| + \|\mathcal{J}_0\|)\|\mathcal{J} - \mathcal{J}_0\|. \tag{91}$$

This shows that the singular values remain smooth provided that $\mathcal{J}_0$ is non-singular and further places the restrictions

$$(\text{Kn}\tau)^2 \ll 1 \tag{92}$$
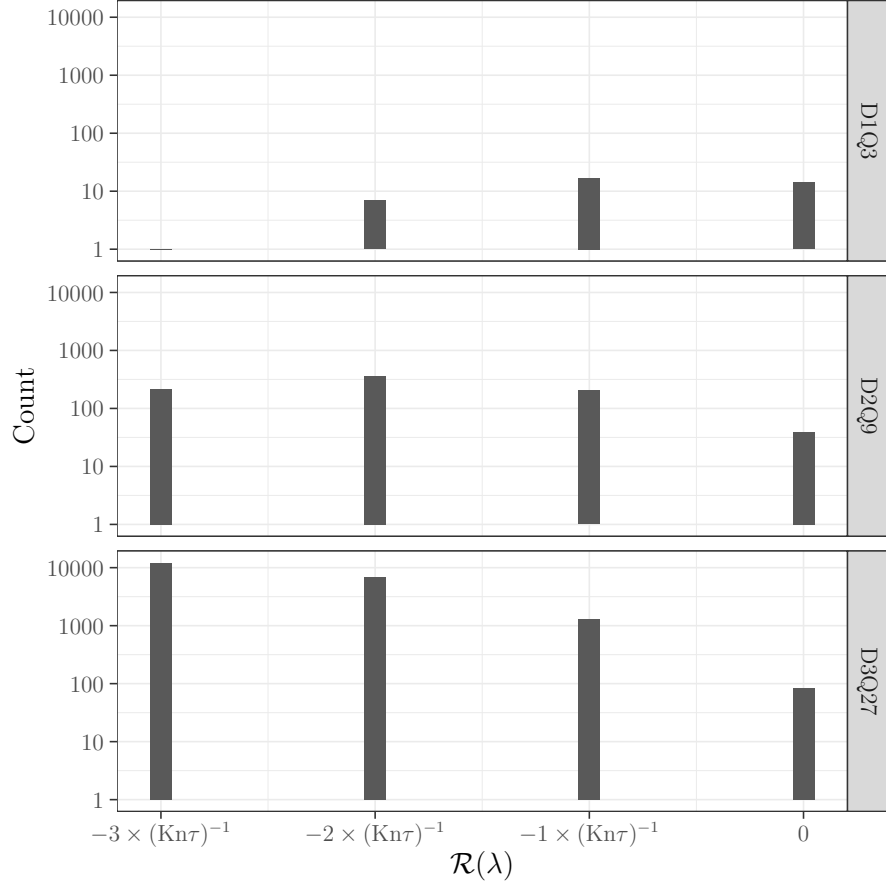
$$(\text{Kn}\tau)^3 \log n \ll 1 \tag{93}$$

FIG. 3. Histograms of eigenvalue spectra $\mathcal{R}(\lambda)$ of 3rd-degree Carleman-linearized D1Q3, D2Q9, and D3Q27 LBM matrices. Up to floating point error $< 10^{-12}$ from the numerical diagonalization, the eigenvalues are all discrete multiples $-\{0, 1, 2, 3\} \times (\mathrm{Kn}\tau)^{-1}$ of the Boltzmann relaxation scale $(\mathrm{Kn}\tau)^{-1}$. Again up to numerical fuzz $< 10^{-13}$, all eigenvalues are purely real.

on the free parameters of the system. The first condition is less restrictive than the $\mathrm{Kn}\tau \ll 1$ condition the system must already satisfy, while the second is unlikely to be a practical impediment for reasonable values of n.

Lastly, we need to bound the effect of the perturbation on $\|\mathcal{J}^{-1}\|$. To accomplish this, we use the approximation

$$\mathcal{J}^{-1} \approx (\mathcal{J}_0 + \mathcal{J}')^{-1} = \mathcal{J}_0^{-1} + \mathcal{J}_0^{-1} \mathcal{J}' \mathcal{J}_0^{-1} \tag{94}$$

where $\mathcal{J}' = \mathcal{J} - \mathcal{J}_0$ is the perturbation to the eigenvectors; since this perturbation scales as $O((\mathrm{Kn}\tau)^2)$, the neglected terms in the expansion of the inverse scale as $O((\mathrm{Kn}\tau)^4)$. By the submultiplicative property of the spectral norm,

$$\|\mathcal{J}^{-1} - J_0^{-1}\| \leq \|\mathcal{J}_0^{-1}\|^2 \|\mathcal{J}'\|. \tag{95}$$

Using $\|\mathcal{J}_0^{-1}\|$ from the block structure of $\mathcal{C}_c$ and $\max_i |\Xi_i'| = O((\mathrm{Kn}\tau)^2)$ from Eq. (87) to bound $\|\mathcal{J}'\|$, we conclude that the n-point $\|\mathcal{J}^{-1}\|$ is also independent of n.

h. *Stability* Matrix stability refers to $\mathcal{R}(\lambda) \leq 0$ and is a necessary condition for the Berry *et al.* [39] algorithm. We now show that $\mathcal{C}$ satisfies that condition if the underlying physical system is linearly stable.

Because of its block triangular structure (in Kronecker degree, not **x**), the eigenvalue problem for $\mathcal{C}$ reduces to

Term	Scaling	Reference
κ_J	$\leq 1.152 \times 10^5$	
$\|\mathcal{C}\|$	$O(\mathrm{Kn}^{-1})$	Eq. (77)
s	$O(1)$	Eq. (75)
g	$O(1)$	Eq. (72)
β	$O(1)$	Eq. (73)

TABLE I. Scaling of each term in Eq. (3) with lattice Boltzmann equation parameters leading to the result of Eq. (101).

finding the eigenvalues of the block-diagonal (in Kronecker degree) elements: the transfer matrices

$$\mathcal{A}_1^1 - \mathcal{B}_1^1 = \mathcal{F}^{(1)} - S \tag{96}$$

$$\mathcal{A}_2^2 - \mathcal{B}_2^2 = \mathbb{I}_{nQ \times nQ} \otimes (\mathcal{F}^{(1)} - S) + (\mathcal{F}^{(1)} - S) \otimes \mathbb{I}_{nQ \times nQ} \tag{97}$$

$$\begin{aligned}
\mathcal{A}_3^3 - \mathcal{B}_3^3 = {}& \mathbb{I}_{nQ \times nQ}^{(2)} \otimes (\mathcal{F}^{(1)} - S) \\
& + \mathbb{I}_{nQ \times nQ} \otimes (\mathcal{F}^{(1)} - S) \otimes \mathbb{I}_{nQ \times nQ} \\
& + (\mathcal{F}^{(1)} - S) \otimes \mathbb{I}_{nQ \times nQ}^{(2)}.
\end{aligned} \tag{98}$$

Denote the eigenvectors and eigenvalues of $\mathcal{F}^{(1)} - S$ as v_i and μ_i ($i \in 1, \ldots, nQ$). It is trivial to show that the eigenvectors and eigenvalues of $(\mathcal{F}^{(1)} - S) \otimes \mathbb{I}_{nQ \times nQ}$ and $\mathbb{I}_{nQ \times nQ} \otimes (\mathcal{F}^{(1)} - S)$ are simply $v^{(2)} = v \otimes v$ and $\mu^{(2)} = \mu_i + \mu_j$ ($i, j \in 1, \ldots, nQ$); similarly for $(\mathcal{F}^{(1)} - S) \otimes \mathbb{I}_{nQ \times nQ}^{(2)}$, etc. Therefore, if all eigenvalues of $(\mathcal{F}^{(1)} - S)$ are nonpositive, the eigenvalues of $\mathcal{C}$ will also be nonpositive.

The stability of $\mathcal{C}$ is thus determined by the stability of $\mathcal{F}^{(1)} - S$. This is equivalent to a linear stability analysis on the lattice Boltzmann system [50]. Linear stability (or a stronger stability criterion) will be satisfied by any physical system to which the quantum solver will be applied, as the simulation would be physically nonsensical otherwise.

i. Evolution time The physical evolution time $\tilde{T}$ is imposed by the nature of the system being simulated. Physical and lattice evolution time are related by the Sterling and Chen [50] factor (Eq. (10)),

$$T = \tilde{T} / \left(\frac{L}{e_r} \right). \tag{99}$$

Final quantum gate complexity to solve Eq. (44)

Finally, inserting Eq. (75)–(99) into Eq. (3) yields the following result for the quantum algorithm complexity as quantified by the number of two-qubit gates needed in the simulation:

$$\text{gate complexity} = O(\mathrm{Kn}^{-1} e_r L^{-1} \tilde{T} \, \text{poly} \log(n/\epsilon)), \tag{100}$$

where $\tilde{T}$ is the physical evolution time, and L and e_r are characteristic scales chosen for the LBE formalism. The scaling of each term in Eq. (3) is summarized in Table I.

The solution error of using the quantum linear system algorithm (QLSA) of Berry *et al.* [39] to solve Eq. (7) come from two sources: the Carleman truncation error and the QLSA error. Since the solution error from QLSA contributes poly($\log(\epsilon)$) to the gate complexity expressed in Eq. (3), we focus on bounding the Carleman truncation error, which is $O(\mathrm{Ma}^2)$. For weakly compressible flow, $\mathrm{Ma} \ll 1$, therefore, the Carleman truncation error is very small. In Liu *et al.* [42], a QLSA with gate complexity scales with T^2 was used due to their time dependent Carleman matrix. A time dependent Carleman matrix requires discretizing time using the forward Euler method, which contributes to the solution error. In contrast, our Carleman matrix $\mathcal{C}$ is constant, which affords us to use the QLSA of Berry *et al.* [39] with a gate complexity scales with T (Eq. (3)). Overall, our method of using QLSA to solve Eq. (4) has yields a gate complexity scaling with poly($\log N$) and T for any arbitrary Reynolds number comparing to Liu *et al.* [42]'s complexity scaling with T^2 for $\mathrm{Re} < \sqrt{2}$.

DISCUSSION

Trading nonlinearity for degrees of freedom

The first step in our process of adapting turbulence to the requirements of quantum algorithms is to use the lattice Boltzmann form of the NSE (see Results). The lattice Boltzmann equation (LBE) is a nondimensionalized form of the Boltzmann equation with discrete velocities and the Bhatnagar–Gross–Krook collision term [45]. It is called "lattice" because it yields Lagrangian-like solutions when solved with first-order spatial and temporal discretization with upwind advection [35] in which the discrete-velocity particles arrive at neighboring grid points after exactly one time step. This solution method is referred to as the lattice Boltzmann method (LBM). For our purpose, the essential characteristics of the LBE are the linear advection term (inherent to the Boltzmann formulation) and the manifest form of the degree of nonlinearity in the collision term (due to the nondimensionalization).

The advection term is linear in the kinetic-theory-motivated LBE because the discrete velocity distributions are advected in space by constant lattice velocities, the analogue of which in the kinetic theory of fluids is the speed of sound. The collision-term nonlinearity is $O(\mathrm{Ma}^2)$, where Ma is the Mach number, defined as the ratio between the characteristic fluid velocity and the speed of sound. This is because the fluid velocity $\mathbf{u}$ is proportional to the first moment of the particle distribution function. In nearly incompressible flows, $\mathbf{u}$ is always small relative to the speed of sound. The nondimensional velocities, which are scaled by the lattice velocity, make the $|\mathbf{u}| = O(\mathrm{Ma})$ scaling explicit.

Thus, the character of the nonlinearity is fundamentally changed between the NSE and LBE. The nonlinearity of the NSE stems from the term $\mathbf{u} \cdot \nabla \mathbf{u}$, and this nonlinearity is characterized by Re. In contrast, the nonlinearity in the LBE stems from $|\mathbf{u}|^2$, and this nonlinearity is characterized by Ma^2. This change is advantageous for high-Re, low-Ma flows, the situation in most geophysical and many engineering applications. However, it comes at the expense of using a large number of discrete lattice velocities to form the quadrature (Q) that simulates the molecular velocity distribution. For instance, to use LBM to simulate three-dimensional NSE, the number of degrees of freedom must be increased by a factor of 27 in the D3Q27 formulation. Here, the number after D stands for the dimension of the system, and that after Q represents the number of discrete lattice velocities in the quadrature. For n grid points, the number of LBE degrees of freedom increases Q-fold to nQ.

The second step in our process of adapting turbulence to the requirements of quantum algorithms is to eliminate the weakened nonlinearity in the lattice Boltzmann formalism using Carleman linearization [47, 48] (see Results). Carleman linearization leads to an infinite-dimensional system of linear differential equations. The system is truncated at a finite degree for practical implementation, resulting in a truncation error. In work that has pursued this avenue [41, 42], the truncation error depends on the degree of nonlinearity in the original equation [42, 47]. For turbulent flows, Liu *et al.* [42] find that the Carleman-linearized Burgers' equation is intractable for quantum algorithms at $\mathrm{Re} \geq \sqrt{2}$. We show, in contrast, that the truncation error for the Carleman-linearized LBE is a power series in Ma, as expected for a system of equations whose nonlinearity is characterized by Ma; therefore, the truncation error is strongly suppressed for weakly compressible flow and becomes independent of Re (see Results).

As discussed in the Results, the lowest Carleman linearization degree that can be used for the LBE is 3 (i.e., terms up to cubic degree in the distribution functions appear in the truncated equations). This degree is also sufficient, as the associated truncation error is of the same order (i.e., Ma^2) as the LBE error in reproducing the NSE [35].

We note one further difference between our analysis and the truncation error analyses of Liu *et al.* [42] and Forets and Pouly [47]. These prior analyses provide error bounds for arbitrary nonlinear differential equations based on the coefficient-matrix norms for the linear and nonlinear terms. Our results provide much tighter error bounds due to two specific properties of the LBE. First, the symmetries of the lattice lead to exact cancellation of certain terms, which makes the truncation error for powers of u identically zero. Second, we benefit from the velocity rescaling on the lattice, which, as discussed earlier, suppresses the nonlinear terms by $O(\mathrm{Ma})$ relative to the linear terms [53].

After Carleman linearization, the final number of degrees of freedom in the LBE is $N = n^3 Q^3 + n^2 Q^2 + nQ = O(n^3 Q^3)$. This is a dramatic increase over the n degrees of freedom required for NSE at the same resolution. However, this is a polynomial increase; if it permits us to take advantage of $O(\log N)$ scaling, then this is a trade-off well worth making.

Quantum speedup for turbulence

Accurate linear approximation of the LBE in hand, we now need to determine whether the $O(\mathrm{poly} \log N)$ scaling of quantum linear systems solvers can be achieved for our particular system of equations [39, 54].

First, it must be possible to load the initial state and extract the final state in at most $O(\mathrm{poly} \log N)$ time. This constraint precludes applying this method to initial-value problems (e.g., numerical weather prediction). However, a vast class of interesting physical applications (e.g., climate projections) are boundary-value problems; for these

problems, the initial distribution can be highly idealized (e.g., as a Gaussian distribution), and the turbulent features can be allowed to spin up over time. Such an initial state can be prepared in the required time using methods such as Kitaev and Webb [55], Grover and Rudolph [56]. The information extracted from the final state needs to fit into a single scalar that results from measuring the expectation value of an operator on the final state. This is because of the infamous output problem in quantum computing [54] wherein the cost of reading the solution from a quantum algorithm is exponentially greater than the cost of finding the quantum solution. This usually occurs when one wishes to learn the entire solution as a quantum state and, thus, is forced to perform quantum state tomography [57]. Expectation values can typically be learned at modest cost by sampling quantities such as the domain-mean flux across a boundary. This is a meaningful quantity that can be extracted from sampling the state and that does not incur the exponential overhead if one is willing to accept errors that are inverse polynomial in the system size.

Second, the quantum solver needs to be able to evolve the initial state to the final state (i.e., the state after an evolution time $\tilde{T}$) in at most $O(\text{poly} \log N)$ time. Here, we make use of the known complexity of state-of-the-art quantum algorithms for ODEs from Berry *et al.* [39]; we eschew existing approaches to nonlinear differential equations that only use forward-Euler discretizations because of our specialized analysis of the error in Carleman linearization. Expressing each factor in the Berry *et al.* [39] complexity formula (Eq. (3)) in terms of the properties of the Carleman-linearized LBE results in the following expression for gate complexity:

$$\text{complexity} = O(t_c^{-1}\tilde{T}\,\text{poly}\log(n/\epsilon)) \tag{101}$$

(see Results). The system parameters that determine the complexity are the number of discrete lattice velocities Q, the LBE collision time scale t_c, the evolution time $\tilde{T}$, and the number of grid points n.

The number of discrete velocities is fixed and independent of other system parameters; as discussed, $Q \leq 27 \ll n$ is widely used in three-dimensional LBM simulations. Evolution time is an external requirement that is determined by the physics problem being solved. Collision time is associated with the molecular nature of the fluid that can be decoupled from the smallest turbulent time scale (here, the Kolmogorov time scale). The resulting complexity scales as $\text{poly} \log(n)$. This opens the possibility of simulating enormous domains while resolving a complex interplay between physics ranging from Kolmogorov to integral scales.

The overall complexity, therefore, can be set to be independent of the NSE nonlinearity (i.e., the Reynolds number). This conclusion is aligned with a fundamental assumption of the NSE: the continuum assumption that the infinitesimal volume of fluid is much larger than that associated with molecules, which allows the molecular details of the fluid to be dropped. Because of this assumption, the degree of nonlinearity in the LBE formulation can be adjusted independently of that in the NSE. This remarkable result comes from the fundamental difference, discussed above, between the Reynolds-type nonlinearity in the original NSE and the Mach-type nonlinearity in their LBE form.

CONCLUSION AND OUTLOOK

We have shown how to use quantum solvers to simulate turbulence. The resulting logarithmic scaling in number of degrees of freedom compares to the polynomial scaling of the gold-standard classical algorithms [20, 58]. (We make no claim that the best known classical algorithms are, in fact, the best possible [59].) This marks an important milestone in understanding turbulence through numerical simulations. Much ground remains to be covered before reaching the ultimate destination of applying this tool to actual complex physical systems; at the same time, previously unthinkable possibilities are now visible on the horizon.

The specific manifestation of turbulence depends sensitively on boundary conditions. We have not considered these in our idealized derivations, but work on doing so is urgently needed. Furthermore, many complex physical systems are heterogeneous, consisting of multiple coupled subsystems and multiple species or thermodynamic phases. There are well-established ways to impose complex boundary conditions and to add phases, phase interactions, phase change, and reactions in the LBM [60–62]. Such schemes, combined with further development based on our results, can be applied to challenging multiphase or reactive flow problems, such as droplet coalescence under turbulence [63, 64] and nanoparticle assembly under an external field that involves a fluid flow [10, 65]. In essence, our method will need to be extended by further increasing the number of degrees of freedom until not just the Kolmogorov scales but even the solid-particle or liquid-droplet microscale is explicitly resolved. A large number of applications have already been simulated using the LBM [9, 61, 66–74], and these could immediately benefit from such work.

More generally, many systems besides the NSE do not meet the linear and nondissipative requirements of quantum algorithms at first glance. There is often a trade-off between linearity and the number of explicit degrees of freedom sampled. The full dimensionality of a molecular dynamics simulation versus the reduced dimensionality of the nonlinear NSE hydrodynamics is a canonical example. Based on our LBE method, it is plausible that—and it should be urgently tested whether—many of the nonlinear multiscale transport phenomena described by the Boltzmann

transport equation would also benefit from a quantum speedup.

---

[1] G. S. Omenn, Grand challenges and great opportunities in science, technology, and public policy, Science **314**, 1696 (2006).

[2] World Climate Research Programme, WCRP Grand Challenges (last accessed 2023–01–20), `https://www.wcrp-climate.org/grand-challenges/grand-challenges-overview`.

[3] National Academy of Engineering, *Grand Challenges for Engineering: Imperatives, Prospects, and Priorities: Summary of a Forum*, edited by S. Olson (The National Academies Press, Washington, DC, 2016).

[4] K. Hasselmann, Stochastic climate models .1. theory, Tellus **28**, 473 (1976).

[5] A. J. Majda and R. Klein, Systematic multiscale models for the tropics, Journal of the Atmospheric Sciences **60**, 393 (2003).

[6] S. Bony, B. Stevens, D. M. W. Frierson, C. Jakob, M. Kageyama, R. Pincus, T. G. Shepherd, S. C. Sherwood, A. P. Siebesma, A. H. Sobel, M. Watanabe, and M. J. Webb, Clouds, circulation and climate sensitivity, Nature Geoscience **8**, 261 (2015).

[7] M. Ghil and V. Lucarini, The physics of climate variability and climate change, Reviews of Modern Physics **92**, 035002 (2020).

[8] S. Gupta, N. Mastrantonas, C. Masoller, and J. Kurths, Perspectives on the importance of complex systems in understanding our climate and climate change-the nobel prize in physics 2021, Chaos **32**, 052102 (2022).

[9] M. Bernaschi, S. Melchionna, and S. Succi, Mesoscopic simulations at the physics-chemistry-biology interface, Reviews of Modern Physics **91**, 025004 (2019).

[10] M. A. Boles, M. Engel, and D. V. Talapin, Self-assembly of colloidal nanocrystals: From intricate structures to functional materials, Chemical Reviews **116**, 11220 (2016).

[11] V. Salzmann, Bastiaan B., M. M. van der Sluijs, G. Soligno, and D. Vanmaekelbergh, Oriented attachment: From natural crystal growth to a materials engineering tool, Accounts of Chemical Research **54**, 787 (2021).

[12] J. J. De Yoreo, P. U. P. A. Gilbert, N. A. J. M. Sommerdijk, R. L. Penn, S. Whitelam, D. Joester, H. Zhang, J. D. Rimer, A. Navrotsky, J. F. Banfield, A. F. Wallace, F. M. Michel, F. C. Meldrum, H. Coelfen, and P. M. Dove, Crystallization by particle attachment in synthetic, biogenic, and geologic environments, Science **349**, aaa6760 (2015).

[13] J. J. De Yoreo, E. Nakouzi, B. Jin, J. Chun, and C. J. Mundy, Spiers memorial lecture: Assembly-based pathways of crystallization, Faraday Discussions **235**, 9 (2022).

[14] W. B. Russel, W. Russel, D. A. Saville, and W. R. Schowalter, *Colloidal dispersions* (Cambridge University Press, 1991).

[15] S. B. Pope, *Turbulent flows* (Cambridge university press, 2000).

[16] E. Bodenschatz, S. P. Malinowski, R. A. Shaw, and F. Stratmann, Can we understand clouds without turbulence?, Science **327**, 970 (2010).

[17] S. C. Sherwood, S. Bony, and J.-L. Dufresne, Spread in model climate sensitivity traced to atmospheric convective mixing, Nature **505**, 37 (2014).

[18] C. S. Bretherton, Insights into low-latitude cloud feedbacks from high-resolution models, Philosophical Transactions of the Royal Society A-Mathematical Physical and Engineering Sciences **373**, 20140415 (2015).

[19] L. J. Donner, T. A. O'Brien, D. Rieger, B. Vogel, and W. F. Cooke, Are atmospheric updrafts a key to unlocking climate forcing and sensitivity?, Atmospheric Chemistry and Physics **16**, 12983 (2016).

[20] M. A. Sprague, S. Boldyrev, P. Fischer, R. Grout, W. I. Gustafson, Jr., and R. Moser, Turbulent flow simulation at the exascale: Opportunities and challenges workshop: August 4-5, 2015, Washington, D.C. (2017).

[21] T. Schneider, J. Teixeira, C. S. Bretherton, F. Brient, K. G. Pressel, C. Schär, and A. P. Siebesma, Climate goals and computing the future of clouds (2017).

[22] G. Berkooz, P. Holmes, and J. L. Lumley, The proper orthogonal decomposition in the analysis of turbulent flows, Annual review of fluid mechanics **25**, 539 (1993).

[23] B. Podvin and Y. Fraigneau, A few thoughts on proper orthogonal decomposition in turbulence, Physics of Fluids **29**, 020709 (2017).

[24] H. Tennekes and J. L. Lumley, *A first course in turbulence* (MIT press, 1972).

[25] P. A. Durbin, Some recent developments in turbulence closure modeling, Annual Review of Fluid Mechanics **50**, 77 (2018), https://doi.org/10.1146/annurev-fluid-122316-045020.

[26] O. Artime and M. De Domenico, From the origin of life to pandemics: emergent phenomena in complex systems, Philosophical Transactions of the Royal Society A-Mathematical Physical and Engineering Sciences **380**, 20200410 (2022).

[27] G. Feingold, A. McComiskey, T. Yamaguchi, J. S. Johnson, K. S. Carslaw, and K. S. Schmidt, New approaches to quantifying aerosol influence on the cloud radiative effect, Proceedings of the National Academy of Sciences of the United States of America **113**, 5812 (2016).

[28] S. Wheatcraft and J. Cushman, Hierarchical approaches to transport in heterogeneous porous media, Reviews of Geophysics **29**, 263 (1991).

[29] K. S. Carslaw, L. A. Lee, L. A. Regayre, and J. S. Johnson, Climate models are uncertain, but we can do something about it, Eos **99**, 10.1029/2018EO093757 (2018).

[30] J. Muelmenstaedt and G. Feingold, The radiative forcing of aerosol-cloud interactions in liquid clouds: Wrestling and embracing uncertainty, Current Climate Change Reports **4**, 23 (2018).

[31] W. Ge, Q. Chang, C. Li, and J. Wang, Multiscale structures in particle-fluid systems: Characterization, modeling, and simulation, Chemical Engineering Science **198**, 198 (2019).

[32] S. C. Sherwood, M. J. Webb, J. D. Annan, K. C. Armour, P. M. Forster, J. C. Hargreaves, G. Hegerl, S. A. Klein, K. D. Marvel, E. J. Rohling, M. Watanabe, T. Andrews, P. Braconnot, C. S. Bretherton, G. L. Foster, Z. Hausfather, A. S. Heydt, R. Knutti, T. Mauritsen, J. R. Norris, C. Proistosescu, M. Rugenstein, G. A. Schmidt, K. B. Tokarska, and M. D. Zelinka, An assessment of earth's climate sensitivity using multiple lines of evidence, Reviews of Geophysics **58**, e2019RG000678 (2020).

[33] N. Bellouin, J. Quaas, E. Gryspeerdt, S. Kinne, P. Stier, D. Watson-Parris, O. Boucher, K. S. Carslaw, M. Christensen, A.-L. Daniau, J.-L. Dufresne, G. Feingold, S. Fiedler, P. Forster, A. Gettelman, J. M. Haywood, U. Lohmann, F. Malavelle, T. Mauritsen, D. T. McCoy, G. Myhre, J. Muelmenstaedt, D. Neubauer, A. Possner, M. Rugenstein, Y. Sato, M. Schulz, S. E. Schwartz, O. Sourdeval, T. Storelvmo, V. Toll, D. Winker, and B. Stevens, Bounding global aerosol radiative forcing of climate change, Reviews of Geophysics **58**, e2019RG000660 (2020).

[34] J. N. Moum, Variations in ocean mixing from seconds to years, Annual Review of Marine Science **13**, 201 (2021).

[35] S. Chen and G. D. Doolen, Lattice boltzmann method for fluid flows, Annual Review of Fluid Mechanics **30**, 10.1146/annurev.fluid.30.1.329 (1998).

[36] S. Orszag and V. Yakhot, Reynolds-number scaling of cellular-automation hydrodynamics, Physical Review Letters **56**, 1691 (1986).

[37] A. W. Harrow, A. Hassidim, and S. Lloyd, Quantum algorithm for linear systems of equations, Phys. Rev. Lett. **103**, 150502 (2009).

[38] D. W. Berry, High-order quantum algorithm for solving linear differential equations, Journal of Physics A: Mathematical and Theoretical **47**, 105301 (2014).

[39] D. W. Berry, A. M. Childs, A. Ostrander, and G. Wang, Quantum Algorithm for Linear Differential Equations with Exponentially Improved Dependence on Precision, Communications in Mathematical Physics **356**, 1057 (2017).

[40] A. M. Childs, R. Kothari, and R. D. Somma, Quantum algorithm for systems of linear equations with exponentially improved dependence on precision, SIAM Journal on Computing **46**, 1920 (2017).

[41] S. Lloyd, G. De Palma, C. Gokler, B. Kiani, Z.-W. Liu, M. Marvian, F. Tennie, and T. Palmer, Quantum algorithm for nonlinear differential equations 10.48550/arXiv.2011.06571 (2020).

[42] J.-P. Liu, H. O. Kolden, H. K. Krovi, N. F. Loureiro, K. Trivisa, and A. M. Childs, Efficient quantum algorithm for dissipative nonlinear differential equations, Proceedings of the National Academy of Science **118**, e2026805118 (2021).

[43] H. Siebert, K. Lehmann, and M. Wendisch, Observations of small-scale turbulence and energy dissipation rates in the cloudy boundary layer, Journal of the Atmospheric Sciences **63**, 1451 (2006).

[44] W. W. Grabowski and L. P. Wang, Growth of cloud droplets in a turbulent environment, Annual Review of Fluid Mechanics **45**, 293 (2013).

[45] P. L. Bhatnagar, E. P. Gross, and M. Krook, A Model for Collision Processes in Gases. I. Small Amplitude Processes in Charged and Neutral One-Component Systems, Physical Review **94**, 511 (1954).

[46] F. Toschi and S. Succi, Lattice boltzmann method at finite knudsen numbers, Europhysics Letters **69**, 549 (2005).

[47] M. Forets and A. Pouly, Explicit error bounds for carleman linearization 10.48550/ARXIV.1711.02552 (2017).

[48] T. Carleman, Application of the theory of linear integration equations to nonlinear systems of differential equations, Acta Mathematica **59**, 63 (1932).

[49] G. K. Batchelor, *An introduction to fluid dynamics* (Cambridge University Press, 2000).

[50] J. D. Sterling and S. Chen, Stability Analysis of Lattice Boltzmann Methods, Journal of Computational Physics **123**, 196 (1996).

[51] Code location for LBM (2023).

[52] J. J. Sakurai, *Modern quantum mechanics; rev. ed.* (Addison-Wesley, Reading, MA, 1994).

[53] P. Lallemand, L.-S. Luo, M. Krafczyk, and W.-A. Yong, The lattice boltzmann method for nearly incompressible flows, Journal of Computational Physics **431**, 109713 (2021).

[54] S. Aaronson, Read the fine print, Nature Physics **11**, 291 (2015).

[55] A. Kitaev and W. A. Webb, Wavefunction preparation and resampling using a quantum computer, arXiv preprint arXiv:0801.0342 (2008).

[56] L. Grover and T. Rudolph, Creating superpositions that correspond to efficiently integrable probability distributions, arXiv preprint quant-ph/0208112 (2002).

[57] M. Cramer, M. B. Plenio, S. T. Flammia, R. Somma, D. Gross, S. D. Bartlett, O. Landon-Cardinal, D. Poulin, and Y.-K. Liu, Efficient quantum state tomography, Nature communications **1**, 1 (2010).

[58] S. Orszag, Analytical theories of turbulence, Journal of Fluid Mechanics **41**, 363 (1970).

[59] E. Tang, Quantum principal component analysis only achieves an exponential speedup because of its state preparation assumptions, Phys. Rev. Lett. **127**, 060503 (2021).

[60] Q. Zou and X. He, On pressure and velocity boundary conditions for the lattice boltzmann bgk model, Physics of Fluids **9**, 1591 (1997).

[61] A. J. C. Ladd and R. Verberg, Lattice-boltzmann simulations of particle-fluid suspensions, Journal of Statistical Physics **104**, 1191 (2001).

[62] Z. Guo, C. Zheng, and B. Shi, Discrete lattice effects on the forcing term in the lattice boltzmann method, Phys. Rev. E **65**, 046308 (2002).

[63] J. Chun, D. L. Koch, S. L. Rani, A. Ahluwalia, and L. R. Collins, Clustering of aerosol particles in isotropic turbulence, Journal of Fluid Mechanics **536**, 219 (2005).

[64] X. Y. Li, A. Brandenburg, G. Svensson, N. E. Haugen, B. Mehlig, and I. Rogachevskii, Effect of turbulence on collisional growth of cloud droplets, Journal of the Atmospheric Sciences **75**, 10.1175/JAS-D-18-0081.1 (2018).

[65] D. A. Saviile, Electrokinetic effects with small particles, Annual review of fluid mechanics **9**, 321 (1977).

[66] N. S. Martys and J. F. Douglas, Critical properties and phase separation in lattice boltzmann fluid mixtures, Phys. Rev. E **63**, 031205 (2001).

[67] L. Chen, Q. Kang, Y. Mu, Y.-L. He, and W.-Q. Tao, A critical review of the pseudopotential multiphase lattice boltzmann model: Methods and applications, International Journal of Heat and Mass Transfer **76**, 210 (2014).

[68] Q. Li, K. Luo, Q. Kang, Y. He, Q. Chen, and Q. Liu, Lattice boltzmann methods for multiphase flow and phase-change heat transfer, Progress in Energy and Combustion Science **52**, 62 (2016).

[69] H. Liu, Q. Kang, C. R. Leonardi, S. Schmieschek, A. Narváez, B. D. Jones, J. R. Williams, A. J. Valocchi, and J. Harting, Multiphase lattice boltzmann simulations for porous media applications, Computational Geosciences **20**, 777 (2016).

[70] Y.-L. He, Q. Liu, Q. Li, and W.-Q. Tao, Lattice boltzmann methods for single-phase and solid-liquid phase-change heat transfer in porous media: A review, International Journal of Heat and Mass Transfer **129**, 160 (2019).

[71] K. J. Petersen and J. R. Brinkerhoff, On the lattice boltzmann method and its application to turbulent, multiphase flows of various fluids including cryogens: A review, Physics of Fluids **33**, 041302 (2021).

[72] R. Samanta, H. Chattopadhyay, and C. Guha, A review on the application of lattice boltzmann method for melting and solidification problems, Computational Materials Science **206**, 111288 (2022).

[73] R. Nourgaliev, T. Dinh, T. Theofanous, and D. Joseph, The lattice boltzmann equation method: theoretical interpretation, numerics and implications, International Journal of Multiphase Flow **29**, 117 (2003).

[74] C. K. Aidun and J. R. Clausen, Lattice-boltzmann method for complex flows, Annual Review of Fluid Mechanics **42**, 439 (2010).

ACKNOWLEDGMENTS